What controls the initial peak of an air gun source signature?

Leighton M. Watson[*], *Jonatan Werpers*[†], *Eric M. Dunham*[*‡]

ABSTRACT

Seismic air guns are broadband sources that generate acoustic waves at many frequencies. The low frequency waves can be used for imaging while the high frequency waves are attenuated and/or scattered before they can reflect from targets of interest in the subsurface. It is desirable to reduce the amplitude of the high frequency acoustic waves as they are thought to be disruptive, and potentially damaging, to marine life and are not useful for geophysical purposes. The high frequency acoustic waves are primarily associated with the initial expansion of the air gun bubble and associated peak in the acoustic pressure time series, **which is** commonly referred to as the source signature of the air gun. Here, we develop a **quasi-one-dimensional** model of a seismic air gun **coupled to a spherical bubble** that accounts for gas dynamics and spatially variable depressurization inside the firing chamber in order to investigate controls on the initial peak of the source signature. **The model is validated against data collected during field tests in Lake Seneca, New York. Simulations and field data both show that the initial peak is primarily dependent on the operating pressure. A lower gun pressure results in a smaller peak amplitude and a slower rise time.** The slope, the amplitude of the initial peak divided by the rise time, is used as a proxy for environmental impact and **can** decrease by **as much as** 50% when the air gun pressure is reduced from 2000 psi to 1000 psi. **The low frequencies are controlled by the total discharged mass, which is dependent upon gun volume and pressure. Decreasing the operating pressure while simultaneously increasing the gun volume will reduce the high frequencies while maintaining the desirable low frequency signals.**

INTRODUCTION

Seismic air guns are the primary acoustic wave source used in marine seismic surveys. An air gun discharges **high pressure** air into the water forming an oscillating bubble that radiates acoustic waves. The waves propagate to the sea-floor and are reflected by layers in the subsurface, illuminating exploration targets. Air guns are typically operated at a firing pressure of 2000 psi and the current commercial guns can have volumes of anywhere between 40 in^3 (0.7 L) to **2000** in^3 (33 L) and lengths **on the order** of 1 m.

Seismic air guns are a broadband source generating signal over a wide range of frequencies. The low frequencies (below ∼100 Hz) are geophysically useful; they coherently penetrate the subsurface and reflect from targets of interest. The higher frequencies, however, are attenuated faster, scattered more by heterogeneous overburden, unable to penetrate as deep (Ziolkowski et al., 2003) **and are of limited benefit to imaging (Coste et al., 2014)**. Furthermore, in conventional seismic acquisition receivers typically sample at 2 ms meaning that any signal above the Nyquist frequency of 250 Hz is not recovered.

Acoustic waves are excited by the volumetric change of the bubble of air that is formed when the air gun discharges. The far-field acoustic pressure, Δp, referred to as the source signature of the air gun, **due to the direct wave from the source to receiver** is given

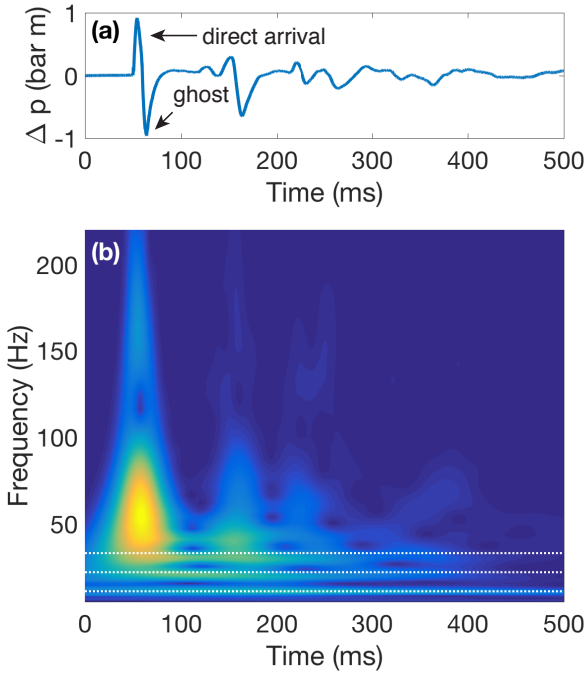

Figure 1: (a) Time series and (b) continuous wavelet transform showing the acoustic pressure in the water, referred to as the source signature of the air gun, measured by a hydrophone 75 m below a 25 in long air gun with a volume of 600 in^3 pressurized to 1030 psi fired at a depth of 7.5 m (Chelminski et al., 0; Ronen and Chelminski, 2018). The horizontal white dotted lines denote the fundamental frequency and first two overtones of the bubble oscillations.

by (Keller and Kolodner, 1956)

$$\Delta p(t,r) = \rho_\infty \frac{\ddot{V}_b(t - r/c_\infty)}{4\pi r} \tag{1}$$

where $V_b = (4/3)\pi R^3$ is the volume of the bubble, **which is assumed to be spherical**, R is the bubble radius, r is the distance from the bubble to the receiver, and c_∞ and ρ_∞ are the ambient speed of sound and density in the water, respectively.

The source signature of an air gun includes both the direct arrivals and the ghost. The direct arrivals are acoustic waves that propagate directly from the source to the receiver and produce the positive peaks in the source signature. The ghost arrivals are initially up-going waves that are reflected from the sea surface with a reflection coefficient of approximately -1 and generate troughs in the far-field acoustic pressure signal. For a receiver directly below the air gun the ghost arrives at **time** $t = 2D/c_\infty$ after the direct arrival, where D is the depth of the air gun.

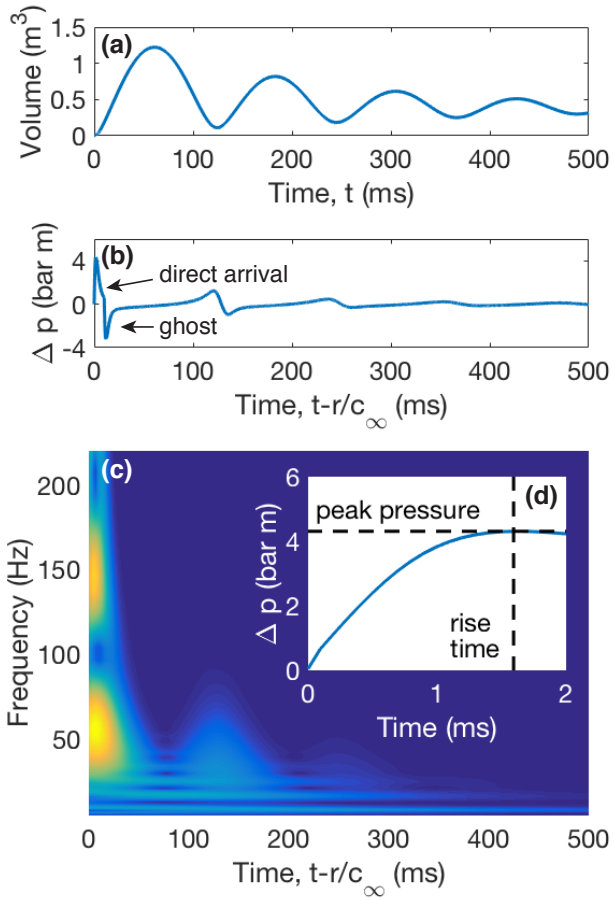

Figure 2: Simulated air gun dynamics showing (a) bubble volume, (b) acoustic pressure time series and (c) continuous wavelet transform. (d) shows the rise time and peak pressure of the first peak in the acoustic pressure time series. Simulation parameters are given in Table 1.

In this manuscript we report the source signature **in units of** bar m. The units of bar m are obtained by multiplying the observed acoustic pressure **measured in bar** by the distance from the air gun to the observation point. This corrects for 1/distance geometrical spreading and allows for comparison of different air gun signals measured at different distances.

The majority of the high frequency signal is associated with the **initial** peak of the source signature (Figures 1 and 2). The initial peak is generated by the discharge of air from the air gun and occurs while the **bubble radius is rapidly expanding but** before the bubble reaches its maximum radius and **typically** before the port closes. The peak acoustic pressure, defined as the maximum amplitude of the first peak in the acoustic pressure time series, is typically reached within several milliseconds of the port opening. The time from the port opening to the peak acoustic pressure is referred to as the rise time and the slope of the initial peak is given by (peak acoustic pressure)/rise time.

There is mounting concern about the impact of seismic surveys on marine life (Gordon et al., 2003; Hildebrand, 2005; Southall et al., 2008; Weilgart, 2013; Nowacek et al., 2015; Williams et al., 2015; McCauley et al., 2017). Marine life, with the exception of whales that communicate with low frequency (15 - 100 Hz) calls (Goldbogen et al., 2014; Stimpert et al., 2015; Watson et al., 2017b), is thought to be most sensitive to the non-geophysically useful high frequency component of air gun signals (Kastelein et al., 2014; Finneran, 2015). Therefore, there is significant interest in modifying existing seismic air gun designs or operating procedures (Coste et al., 2014; Chelminski et al., 0), or designing new marine seismic sources such as marine vibrators (Pramik et al., 2015), in order to reduce the amplitude of the high frequency components of the signal and minimize the environmental impact of marine seismic surveys. The amplitude of high frequency acoustic waves is related to the slope of the initial acoustic pressure pulse **(Coste et al., 2014)**. A source signature with a steeper slope will consist of more signal at high frequencies. Therefore, the slope can be used as a proxy for environmental impact (Chelminski et al., 0; Ronen and Chelminski, 2018).

In this work we develop **a coupled model of a seismic air gun and bubble** that accounts for depressurization inside the air gun. **The model is validated against field data.** We examine the factors that control the initial peak of the source signature, which is associated with the high frequency acoustic waves, with the goal of informing future air gun design and operation.

MODEL

A complete model of the source signature generated by a seismic air gun consists of three components: an air gun model, a bubble model, and an acoustic wave propagation model. The modeling advance presented here is the development of a quasi-1D description of gas dynamics within the air gun chamber accounting for flow and spatially variable depressurization.

There is a substantial body of literature on modeling seismic air gun signatures. **Ziolkowski (1970) performed the seminal work by using results from underwater explosion research (Gilmore, 1952) to model the air bubble and acoustic waves generated by an air gun. Ziolkowski (1970) idealized the bubble as spherically symmetric and utilized a lumped parameter model where the internal properties of the bubble, such as pressure and density, are described by a single time-varying value. Subsequently, numerous authors have utilized this modeling framework and compared their simulation results to field data (Landrø and Sollie, 1992; Laws et al., 1998) and laboratory experiments (Langhammer and Landrø, 1996; Li et al., 2010; de Graaf et al., 2014a).**

The initial simulations of Ziolkowski (1970) over predicted the amplitude of the source signature and, without artificial damping, under predicted the decay rate of the bubble oscillation amplitude. Multiple studies have examined potential damping mechanisms including heat conduction (Li et al., 2010), heat transfer via evaporation and condensation (Ziolkowski, 1982; Ziolkowski and Metselaar, 1984), magnification of the bubble surface area due to turbulence (Ziolkowski and Metselaar, 1984; Laws et al., 1990), mechanical energy dissipation from turbulence (Langhammer and Landrø, 1996), and viscosity (Langhammer and Landrø, 1993). A summary of potential damping mechanisms is provided by de Graaf et al. (2014b).

The lumped parameter assumption **pioneered by Ziolkowski (1970)** where bubble and air gun properties are assumed to be spatially uniform is a useful **approximation** as it reduces the complexity of the system and allows the dynamics **of the system** to be described by a system of ordinary differential equations while still capturing much of the essential physics. Lumped parameter models are computationally cheap and sufficiently simple that they can help to garner an intuitive understanding of the system. In contrast, allowing for spatial variability in properties requires solving a system of partial differential equations, **which must be solved using more expensive computational fluid dynamics simulations.** However, it is only appropriate to approximate a spatially variable property with a single value when the time taken for a wave to propagate across the domain is small compared to the characteristic time scale of the dynamics. If this is the case, spatial variations in properties are rapidly smoothed out throughout the domain before they can affect the dynamics of the system. **However,** if this is not the case then describing the system with a lumped parameter model can neglect significant behavior of the system that is induced by the spatially variable properties.

Seismic air gun bubbles have a typical **equilibrium** diameter of 1 m and oscillate with a period of approximately 0.1 s, although these values **depend upon the bubble depth and mass of air in the bubble, the latter of which is controlled by air gun volume and operating pressure.** The time taken for an acoustic wave to propagate across a 1

m diameter bubble, assuming a velocity of sound in air of 340 m/s, is 3 ms, which is small (3%) compared to the oscillation period. Hence, a lumped parameter bubble model of the bubble is **likely to be** an appropriate description.

Conventional seismic air guns are typically **on the order of** 1 m in length. The characteristic time scale of the air gun dynamics is the **firing time. The port is triggered electronically to open at a specified time and closes when the chamber pressure drops to a sufficiently low value. The port closes while the pressure inside the air gun is greater than the ambient pressure in order to prevent water flooding the gun.** In this work we specify a firing time of 10 ms. The time scale of wave propagation across the air gun is comparable (30%) to the discharge time, suggesting that a lumped parameter description of the air gun may neglect important air gun dynamics, although this will vary between air guns depending on the length of the firing chamber and discharge time. **Accounting for internal gas dynamics will be especially important for the extremely large (multiple meters long) sources proposed by Chelminski et al. (0).**

Recent work has focused on sophisticated computational-fluid-dynamics (CFD) modeling methods. King et al. (2015) developed a 2D axisymmetric finite-volume scheme that was used by King (2015) to model bubble dynamics and investigate departures from spherical symmetry caused by bubble-ghost interactions. Coste et al. (2014), Gerez et al. (2015) and Groenass et al. (2016) performed high-fidelity 3D simulations of air gun/bubble dynamics, which were used to aid the design of a new air gun that generated less high frequency noise.

In this manuscript we develop a quasi-1D model of flow inside the air gun that is fully coupled to a spherically symmetric/lumped parameter description of the bubble (Figure 3). The model is used to investigate controls on the initial peak of an air gun signature, **specifically the role of spatially variable depressurization inside the air gun. This work is complementary to that of King (2015) as we focus on flow inside the air gun whereas King (2015) concentrated on simulating the bubble dynamics. The model presented here fills a niche between the well studied lumped parameter models (e.g., de Graaf et al., 2014b) and computationally expensive CFD simulations. Our model runs in seconds on a desktop computer compared to the weeks required by the 3D CFD models (Groenass et al., 2016).**

Lumped Parameter Model

Much of the previous modeling work on seismic air gun signatures uses a lumped parameter modeling framework (e.g., Ziolkowski, 1970; Laws et al., 1990; Landrø and Sollie, 1992; Li et al., 2010; de Graaf et al., 2014b; Li et al., 2014). Thus, we first present a lumped parameter model of the air gun/bubble system that will later be compared against our 1D air gun model. In the lumped parameter framework the properties of the air gun and bubble are described by a single value, for example pressure or temperature, that varies in time but has no spatial dependence. Therefore, the air gun and bubble models can be written as a system of ordinary differential equations.

Air Gun

In the lumped parameter air gun model, we keep track of the pressure, p_a, mass, m_a, temperature, T_a, and internal energy, E_a, of the gas inside the air gun. The air gun has volume V_a. The air obeys the ideal gas equation of state,

$$p_a = \frac{m_a Q T_a}{V_a}, \tag{2}$$

where Q is the specific gas constant (for dry air Q=287.06 J/kg/K), and internal energy is

$$E_a = c_v m_a T_a, \tag{3}$$

where c_v is the heat capacity at constant volume.

When the port is open, mass flows from the air gun into the bubble according to (Chapman, 2000; Chelminski et al., 0)

$$\frac{dm_a}{dt} = \begin{cases} 0 & \text{if port is closed,} \\ p_a A \left(\frac{\gamma}{QT_a}\right)^{\frac{1}{2}} \left(\frac{2}{\gamma-1}\right)^{\frac{1}{2}} \left[\left(\frac{p_a}{p_b}\right)^{\frac{\gamma-1}{\gamma}} - 1\right]^{\frac{1}{2}} & \text{if flow is unchoked,} \\ p_a A \left(\frac{\gamma}{QT_a}\right)^{\frac{1}{2}} & \text{if flow is choked,} \end{cases} \tag{4}$$

where A is the port area, p_b is the bubble pressure, and γ is the ratio of heat capacities ($\gamma = 1.4$ for diatomic gases such as air). Flow is choked (velocity equal to speed of sound) if the pressure ratio across the port exceeds a critical value given by (Chapman, 2000; Babu, 2014)

$$\frac{p_a}{p_b} > \left(\frac{\gamma+1}{2}\right)^{\frac{\gamma}{\gamma-1}} \tag{5}$$

and the speed of sound is given by

$$c = \left(\frac{\gamma p}{\rho}\right)^{1/2} = (\gamma Q T)^{1/2}. \tag{6}$$

The internal energy of the air gun, E_a, evolves according to

$$\frac{dE_a}{dt} = c_p T_a \frac{dm_a}{dt}. \tag{7}$$

where $c_p = \gamma c_v$ is the heat capacity at constant pressure.

Bubble

The bubble is **idealized** as spherically symmetric with spatially uniform internal properties. The bubble wall dynamics are governed by the modified Herring equation (Herring, 1941; Cole, 1948; Vokurka, 1986; Appendix A):

$$R\ddot{R} + \frac{3}{2}\dot{R}^2 = \frac{p_b - p_\infty}{\rho_\infty} + \frac{R}{\rho_\infty c_\infty}\dot{p_b} - \alpha\dot{R}, \tag{8}$$

where R and $\dot{R} = dR/dt$ are the radius and velocity of the bubble wall, respectively, and p_∞, ρ_∞ and c_∞ are the ambient pressure, density, and speed of sound, respectively, in the water infinitely far from the bubble. The ambient pressure is calculated by adding the hydrostatic pressure to the atmospheric pressure, $p_\infty = p_{\text{atm}} + \rho_\infty g D$, where p_{atm} is the atmospheric pressure, g is the acceleration from gravity and D is the depth of the air gun below the water. Numerical models of air gun signatures typically underpredict the damping observed in the data. This is likely due to the models neglecting various dissipation mechanisms such as turbulence and energy loss to phase changes. Mechanical energy dissipation mechanisms, which are challenging to model directly, are parameterized into an extra damping term of the form of $-\alpha\dot{R}$ where α is an empirically determined constant (Langhammer and Landrø, 1996; Watson et al., 2017a). This term dampens the bubble oscillations so that they are in agreement with the observations but has minimal impact on the initial bubble growth.

The pressure in the bubble is calculated from the ideal gas equation of state,

$$p_b = \frac{m_b Q T_b}{V_b}, \tag{9}$$

where m_b is the mass inside the bubble, T_b is the temperature inside the bubble in Kelvin, and V_b is the volume of the spherical bubble and the internal energy is

$$E_b = c_v m_b T_b. \tag{10}$$

The air gun and bubble are coupled by conservation of mass at the port:

$$\frac{dm_b}{dt} = -\frac{dm_a}{dt}. \tag{11}$$

The internal energy of the bubble changes due to the advection of mass and associated transport of enthalpy into the bubble, work done by volume changes, and heat loss to the water:

$$\frac{dE_b}{dt} = c_p T_a \frac{dm_b}{dt} - 4\pi M \kappa R^2 (T_b - T_\infty) - p_b \frac{dV_b}{dt}, \tag{12}$$

where T_∞ is the ambient temperature in the water, κ is the heat transfer coefficient (Ni et al., 2011; de Graaf et al., 2014b) and M is a dimensionless, empirically determined constant that accounts for the increased effective surface area over which heat transfer can occur as a result of turbulence in the bubble dynamics (Laws et al., 1990). Equation 12 is a statement of the first law of thermodynamics for an open system (Tolhoek and de Groot, 1952).

Wave Propagation

Acoustic waves in the water are generated by the expansion and contraction of the bubble. Here, we describe the bubble as a monopole source that excites acoustic waves by unsteady volumetric changes. The acoustic pressure is a superposition of the direct arrival (equation 1) and the ghost, which is an initially upwards propagating wave that is reflected from the surface of the water and arrives at the receiver at a later time:

$$\Delta p(t, r) = \frac{\rho_\infty}{4\pi}\left[\frac{\ddot{V}_b(t - r/c_\infty)}{r} - \frac{\ddot{V}_b(t - (r + 2D)/c_\infty)}{r + 2D}\right], \tag{13}$$

where r is the distance from the air gun to the receiver. The first term on the right corresponds to the direct arrival and the second term to the ghost. The receivers are directly below the air gun. This is the geometry used in the validation against the field data. We assume that the water surface has a reflectivity of -1 (Ziolkowski, 1982), although we note that the reflectivity can be frequency dependent, especially in rough seas (Orji et al., 2013; Klüver and Tabti, 2015).

Other acoustic source mechanisms, such as a dipole source where there are volume preserving oscillations in bubble shape, cannot be described with a lumped parameter model.

Initial Conditions

The air gun and bubble dynamics are governed by a system of ordinary differential equations and a set of initial conditions is required to solve the system of equations. The modified Herring equation (equation 8) has a singularity at $R = 0$. Therefore, following the treatment of Ziolkowski (1970), the bubble is initialized with a non zero radius:

$$R(0) = \left(\frac{3V_0}{4\pi}\right)^{\frac{1}{3}}, \tag{14}$$

where $R(0)$ is the initial radius of the bubble, respectively, and V_0 is the specified initial bubble volume. The conventional choice is to set the initial bubble volume equal to the volume of the air gun (Ziolkowski, 1970; Li et al., 2010; de Graaf et al., 2014b). Here, we use a constant value of V_0= **600** in^3 **to isolate the effect of varying air gun parameters from changing the initial conditions**. The sensitivity of the solution to the **initial bubble volume** is discussed later in the manuscript. The velocity of the bubble wall is initially assumed to be zero and the initial temperature and pressure inside the bubble are equal to the ambient values in the water:

$$\dot{R}(0) = 0, \tag{15}$$

$$T_b(0) = T_\infty, \tag{16}$$

$$p_b(0) = p_\infty = p_{\text{atm}} + \rho_\infty g D. \tag{17}$$

The initial air gun pressure is set equal to the operating pressure, p_0, and the initial temperature is assumed to have equilibrated with the ambient temperature T_∞ (since the air travels a long distance in a submerged umbilical hose from the compressor on the seismic vessel to the air gun):

$$p_a(0) = p_0, \tag{18}$$

$$T_a(0) = T_\infty. \tag{19}$$

The initial mass and internal energy can then be obtained from equations 2 and 3.

1D Air Gun Model

As an alternative to the lumped parameter air gun model of the previous section, we introduce here a quasi-one-dimensional air gun model. A quasi-1D treatment of gas dynamics within narrow pipes, like an airgun, is typical in fluid dynamics (Chapman, 2000; Babu, 2014). The quasi-1D approximation is well justified when the pipe radius is much smaller than axial length scales of interest, which is generally the case for air guns. While this is an approximation, it is a useful one that allows us to gain many insights about how the air gun length, operating pressure, etc., influence the source signature. While no approximation (or model) is perfect, we argue, based on comparisons with data later in this work, that insights drawn from our simulations are robust and will be confirmed in fully 3D CFD simulations (which are obviously much more computationally expensive).

The air gun firing chamber is idealized as a cylinder of length L and cross-sectional area A. The air inside is compressible and inviscid. We only consider waves and flow along the length of the firing chamber, which are governed by the one-dimensional Euler equations:

$$\frac{\partial \rho}{\partial t} + \frac{\partial (\rho v)}{\partial x} = 0, \tag{20}$$

$$\frac{\partial (\rho v)}{\partial t} + \frac{\partial (\rho v^2 + p)}{\partial x} = 0, \tag{21}$$

$$\frac{\partial e}{\partial t} + \frac{\partial [(e + p)v]}{\partial x} = 0, \tag{22}$$

where ρ, p, and v are the density, pressure, and axial velocity of the fluid inside the air gun, respectively, and e is the internal energy per unit volume. The system is closed with the ideal gas equation of state, written here as

$$p = (\gamma - 1)\left(e - \frac{1}{2}\rho v^2\right), \tag{23}$$

and the internal energy per unit volume is

$$e = c_v \rho T. \tag{24}$$

Initial conditions are identical to those in the lumped parameter air gun model, with all fields assumed to be spatially uniform. The 1D air gun model also requires boundary conditions. At the back wall of the air gun, $x = 0$, a solid wall boundary condition, $v(0) = 0$, is imposed. At the air gun port, $x = L$, the boundary condition depends upon the flow state. If flow out of the port is subsonic, $v(L) < c(L)$, continuity of pressure is required and the pressure in the air gun at the port, $p(L)$, is set equal to the pressure in the bubble, p_b. If the port is choked, $v(L) = c(L)$, waves cannot propagate upstream from the bubble into the air gun and **pressure continuity is not required. The bubble pressure will be different than the air gun pressure. The latter is generally the case in our simulations.**

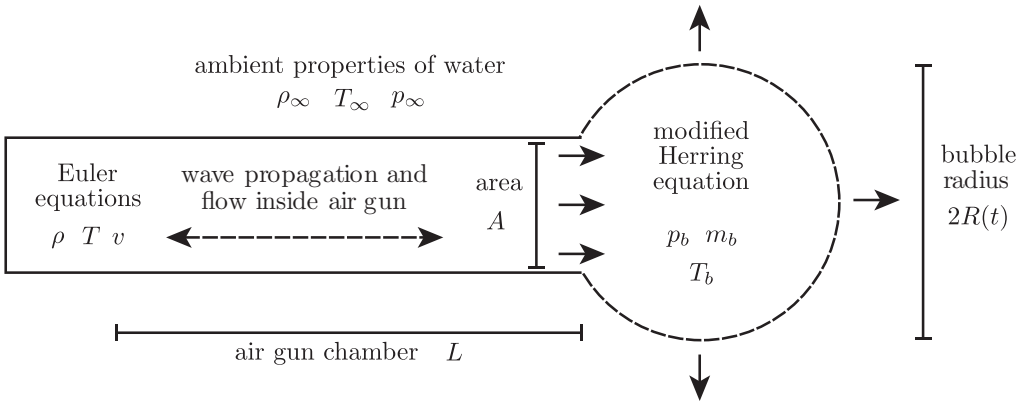

Figure 3: Schematic diagram of the coupled air gun/bubble model.

Bubble

The bubble model that is coupled to the 1D air gun is the same model used in the lumped parameter simulations (equations 8 - 12) with the exception that the rate of mass flow into the bubble is determined by conservation of mass of the gas exiting the air gun:

$$\frac{dm_b}{dt} = v(L)\rho(L)A. \tag{25}$$

The cross-sectional area of the port is assumed to be the same as the cross-sectional area of the firing chamber **(Figure 3)**. **This simplification is discussed later in the manuscript**. **Note also that the port is located at the end of the air gun, which is the source design used in the Lake Seneca field experiments (Chelminski et al., 0) that we use for validation at the end of this study. Many commercial guns have ports located in the middle of the gun (e.g., de Graaf et al., 2014a). The model presented here could be extended to guns with ports in the middle by modeling two air gun chambers, one of either side of the port.** The port is assumed to open and close instantaneously at specified times.

Numerical Implementation

The Euler equations inside the air gun are solved using finite difference summation-by-parts operators for spatial derivatives (Svärd and Nordström, 2014). The air gun and bubble governing equations are evolved in time using an explicit adaptive **Runge-Kutta** (4,5) method. The air gun and bubble models are coupled at the interface using the simultaneous-approximation-term framework (Carpenter et al., 1994; Del Rey Fernández et al., 2014; Svärd and Nordström, 2014). The reader is referred to Appendix B for more details.

AIR GUN DYNAMICS

In this section we simulate the dynamics of an air gun using the 1D air gun model described above. **Parameter values are chosen for later comparison with field data.** We consider a **1.2** m air gun with a cross-sectional area of **12.5** in^2 (corresponding to a gun volume of 600 in^3) suspended in the water at a depth of 7.5 m. The air gun is pressurized to 2000 psi (13.8 MPa). The air inside the air gun is initially at rest and assumed to have equilibrated with the ambient temperature in the water, taken to be 15°C. At $t = 0$ the port located at $x = 1.2$ m opens instantaneously. The pressure in the air gun is significantly higher than the pressure in the water (2000 psi compared to 25 psi at a depth of 7.5 m) and therefore, the air rapidly accelerates and quickly reaches the sonic velocity at the port. Mass flow out of the air gun continues until the port is closed at $t = 10$ ms.

Opening the port causes a rapid pressure drop and creates a rarefaction or depressurization wave that propagates through the air gun firing chamber **(Figure 4)**. As the rarefaction wave propagates through the chamber the density and pressure in the air gun decrease while the velocity increases.

Analytical expressions describing the depressurization of the air gun can be obtained by considering the classic shock tube problem (Laney, 1998; Chapman, 2000) **with the choked flow condition, $v = c$, at the port**. We denote the initial pressure and density of gas in the air gun by p_0 and ρ_0, respectively. The leading edge of the rarefaction wave propagates away from the port at the initial speed of sound, $c_0 = \sqrt{\gamma p_0/\rho_0}$. Within the expansion fan between the leading edge of the rarefaction wave and the air gun port, fluid

Parameter	Description	Value
Air gun:		
p_0	Operating pressure	13.8 MPa = 2000 psi
L	Length	1.2 m
D	Depth	7.5 m
A	Cross-sectional area	12.5 in^2
t_{open}	Time that port is open for	10 ms
Bubble:		
V_0	Initial bubble volume	**600** in^3
M	Magnification of surface area	10
κ	Heat transfer coefficient	4000 $\text{W/m}^2\text{K}$
α	Damping parameter	0.8 m/s
Other:		
ρ_∞	Ambient density in water	1000 kg/m^3
c_∞	Ambient speed of sound in water	1482 m/s
T_∞	Ambient temperature of water	15°C
p_{atm}	Atmospheric pressure	1×10^5 Pa = 14.5 psi
r	Distance from source to receiver	75 m

Table 1: List of parameter values. All simulations use these parameter values unless otherwise stated.

properties vary smoothly according to:

$$v(x,t) = \frac{2}{\gamma+1}\left(c_0 - \frac{L-x}{t}\right), \tag{26}$$

$$c(x,t) = v(x,t) + \frac{L-x}{t}, \tag{27}$$

$$p(x,t) = p_0\left(\frac{c(x,t)}{c_0}\right)^{2\gamma/(\gamma-1)}, \tag{28}$$

$$\rho(x,t) = \frac{\gamma p(x,t)}{c(x,t)^2}, \tag{29}$$

while outside of the expansion fan ($x < L - c_0 t$) the fluid properties are equal to the initial values, $v = 0, c = c_0, p = p_0$ and $\rho = \rho_0$. Within the expansion fan the solution is self-similar in the similarity variable $(L-x)/t$ = (distance from port)/time.

Figure 5 shows that the analytical solution is **an exact match to the numerical simulation, apart from numerical errors associated with the discretization and weak enforcement of the boundary conditions (Appendix B),** while the rarefaction is propagating away from the port. At $t \approx L/c_0 = 3.5$ ms the rarefaction wave reflects off the solid wall at $x = 0$ and propagates back towards the air gun port. After this time the analytical and numerical solutions begin to diverge starting near the back wall of the air gun. This is expected because the analytical solution does not account for the finite length of the air gun **and hence does not include** the reflection of the rarefaction from the back wall.

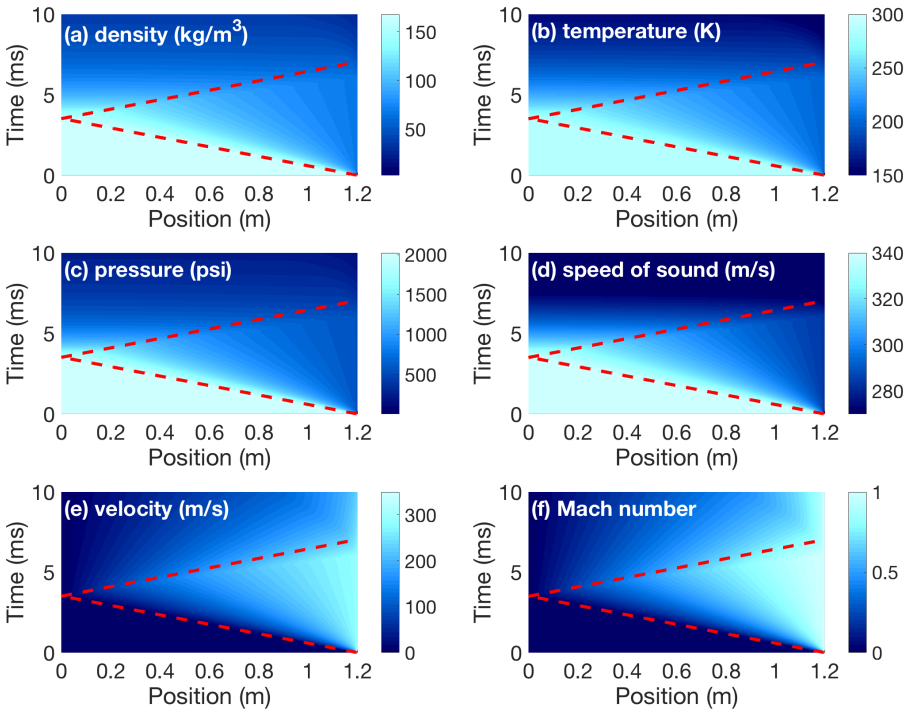

Figure 4: Space-time plots of properties inside the air gun during discharge. The red dashed line indicates a sound wave propagating at the initial sound speed, c_0.

The pressure and density in the air gun at the port decrease and the velocity increases rapidly when the port opens and then the flow chokes. Thereafter, air gun properties at $x = L$ remain at constant values for several milliseconds (Figure 6). **While the port is choked waves cannot propagate up-flow from the bubble into the air gun. During this time the bubble does not influence the dynamics of the air gun.** Analytical solutions for the constant values of pressure, density, velocity and speed of sound

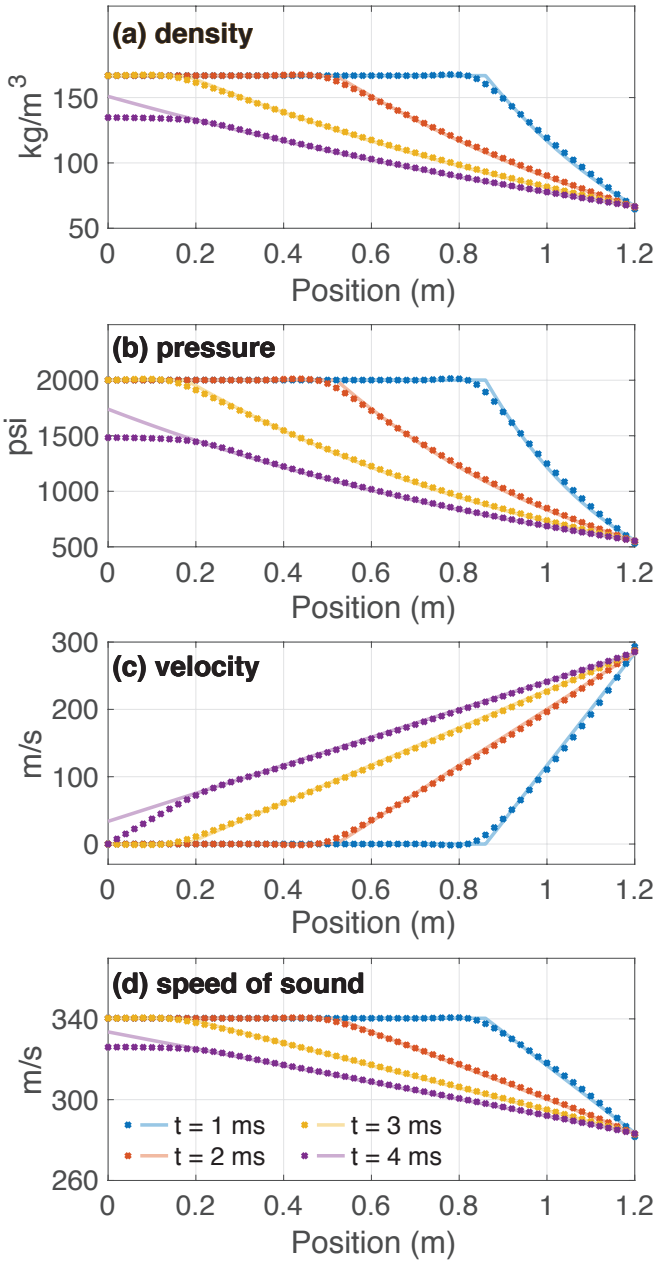

Figure 5: Analytical (solid line) and numerical (crosses) solutions at several times during air gun discharge. Solutions are in good agreement prior to the reflection of the rarefaction from the back wall of the air gun at $t = 3.5$ ms.

at the port can be obtained by evaluating equations 26-29 at $x = L$:

$$v_e(L,t) = \frac{2}{\gamma+1}c_0, \tag{30}$$

$$c_e(L,t) = v_e(L,t), \tag{31}$$

$$p_e(L,t) = p_0\left(\frac{2}{\gamma+1}\right)^{2\gamma/(\gamma-1)}, \tag{32}$$

$$\rho_e(L,t) = \frac{p_0}{c_0^2}\gamma\left(\frac{2}{\gamma+1}\right)^{2/(\gamma-1)}. \tag{33}$$

The numerical and analytical solutions at the port diverge when the rarefaction wave

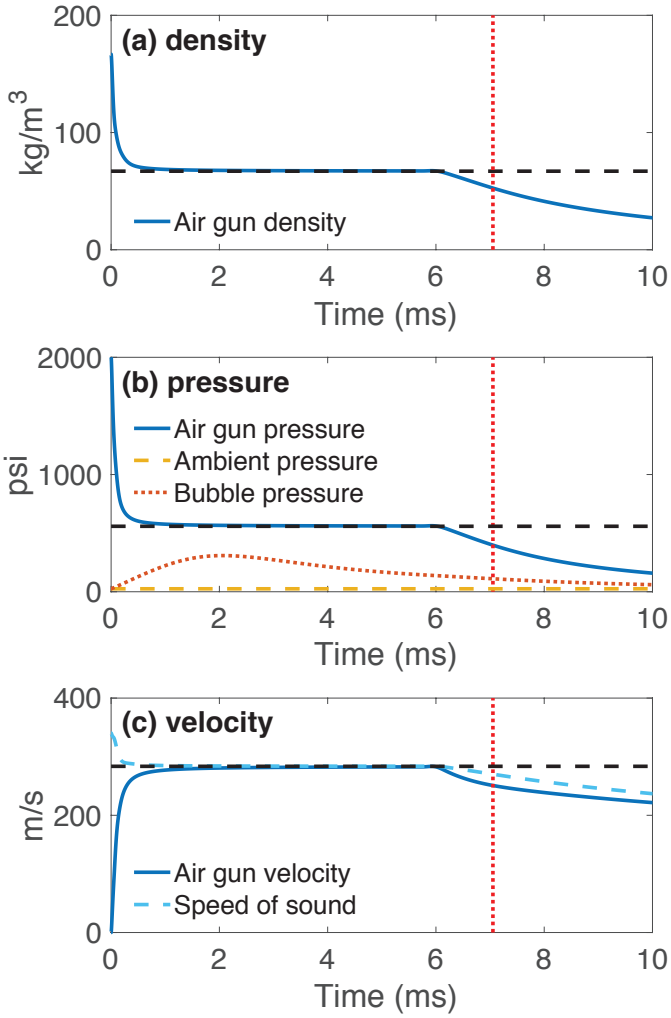

Figure 6: Time series of air gun properties (blue, solid) evaluated at the port, $x = 1.2$ m, during discharge and analytical solutions (black, dashed). **The port opens at time $t = 0$ ms and is closed at $t = 10$ ms.** Vertical red dashed line is at $t = 2L/c_0$. The difference between the numerical and analytical solution in the first ∼1 ms is due to numerical discretization and vanishes with mesh refinement (Appendix B).

propagates back to the port after being reflected by the solid wall at the end of the air gun. The **arrival of the reflected** rarefaction causes the pressure at the air gun port to drop below the sonic solution given by equation 32. Correspondingly, the density and velocity decrease as there is less of a pressure difference across the air gun port to drive flow. The air gun properties continue to decrease until the port is closed at $t = 10$ ms. Practically, the port is closed well before the pressure inside the air gun drops below the ambient pressure in order to prevent water flooding the air gun chamber. **In our simulations** the time scale of the transient dynamics from the initial conditions to the sonic solution is controlled by the grid spacing of the spatial discretization. For more details the reader is referred to Appendix B.

The rarefaction wave arrives back at the port before a wave traveling at a velocity of c_0 would (Figure 6). This is because the rarefaction wave travels at the speed of sound, c, plus the velocity of the air flowing out of the air gun, v. When the rarefaction wave propagates away from the port it is traveling in the opposite direction to the air flow and therefore travels slower than the sound speed with velocity $v - c$. However, when the rarefaction reflects from the back of the firing chamber it propagates in the same direction as the air flow and has a velocity of $v + c$. The velocity inside the air gun reaches an appreciable fraction of the sound speed and offsets the decrease in sound speed due to the depressurization of the air gun **such that the leading edge of the rarefaction returns to the port before time** $t = 2L/c_0$**.**

Comparison to Lumped Parameter Model

In this section we compare the 1D air gun model to the lumped parameter model (Figure 7). We consider two air guns, 0.6 m and 1.2 m long. Both guns have a cross-sectional area of 12.5 in^2 and therefore volumes of 300 in^3 and 600 in^3, respectively.

The lumped parameter model predicts that the pressure at the port will decrease at a slower rate than in the Euler air gun model. This is because the lumped parameter model only considers the average pressure in the air gun whereas the Euler model can account for decreased pressure at the port while the pressure at the other end of the air gun remains at a higher value. The increased pressure at the port means that the lumped parameter model ejects more mass from the air gun prior to the port closing. This results in a bubble that expands faster, generating a larger pressure perturbation with a faster rise time. **In addition, it means that bubble equilibrium radius is larger and hence the bubble oscillates slower (Rayleigh, 1917; Willis, 1941; Watson et al., 2016).**

de Graaf et al. (2014b) conducted laboratory measurements of a seismic air gun as well as lumped parameter modeling of the source signature. Despite matching the bubble period well, their lumped parameter model over-predicted the peak acoustic pressure by 40%. de Graaf et al. (2014b) hypothesized that the discrepancy between data and model could be due to the unmodeled internal complexities of flow passages within the air gun. Our modeling work suggests that the observed discrepancy between data and peak amplitude predicted by a lumped parameter model might be explained by accounting for gas dynamics and spatially variable depressurization inside the air gun firing chamber.

The differences between the lumped parameter model and the 1D air gun model are less

significant when considering the coda of the source signature, especially for small air guns. For a 0.6 m long air gun, by the end of the discharge at $t = 10$ ms the spatially variable properties in the 1D air gun model average out so that a similar mass is ejected from the air gun as for the lumped parameter model (0.73 kg for 1D air gun model compared to 0.77 kg for lumped parameter model). Therefore, the bubble oscillation period is similar for the two models. However, for a 1.2 m long air gun at the end of the discharge time there are still significant spatial variations in air gun properties and hence in mass ejected from the air gun (1.2 kg for 1D air gun model compared to 1.4 kg for lumped parameter model).

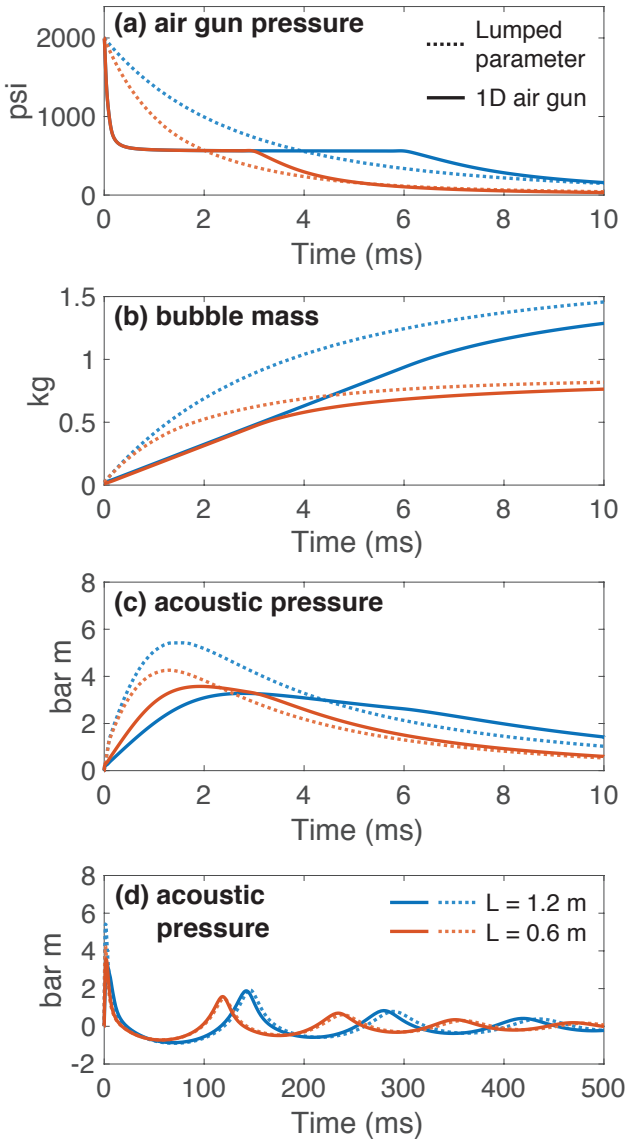

Figure 7: Simulations using the Euler air gun model (solid) and lumped parameter model (dashed) for an air gun with length of 0.6 m (red) and 1.2 m (blue). (a) Air gun pressure at the port during discharge. (b) Bubble mass. (c) Initial stages of the direct acoustic pressure. (d) Extended time series of (c) showing the initial peak and subsequent bubble oscillations.

Lumped parameter models are generally appropriate for modeling the **bubble oscillation component** of the source signature **for small volume guns. However, neglecting spatially variable depressurization inside the air gun can lead to significant over estimation over the peak amplitude and, for large guns, the period of the bubble oscillations.**

Controls on Source Signature

Here, we use our quasi-1D air gun model to investigate controls on the source signature of an air gun. We divide the source signature into two parts: the initial peak and the later bubble oscillations. We focus on tunable operating and design parameters, such as air gun pressure and depth, rather than on physical parameters like the heat transfer coefficient.

Initial Peak

Several factors control the amplitude and shape of the initial peak of an air gun source signature. Here, we **focus on** the impact of air gun pressure, depth and length. The initial peak is strongly dependent on air gun pressure, with a greater initial pressure producing a larger peak acoustic pressure (Figure 8), but relatively insensitive to air gun depth (Figure 9) or, for long guns, length (Figure 10).

The expansion of the bubble is driven by the pressure difference between the pressure inside the bubble and the ambient pressure in the water, $p_b - p_\infty$. The pressure in the bubble is proportional to the mass of the bubble, $p_b = m_b Q T_b / V_b$. An analytical expression for the mass flow rate out of the air gun into the bubble, **which is valid only until the arrival of the reflected rarefaction at the port**, can be derived from equations 30 and 33:

$$\frac{dm_b}{dt} = \rho_e(L,t) v_e(L,t) A, \tag{34}$$

$$= A p_0 \left(\frac{\gamma}{Q T_\infty}\right)\left(\frac{2}{\gamma+1}\right)^{(\gamma+1)/(\gamma-1)}. \tag{35}$$

Equation 35 shows that the mass flow rate out of the air gun is controlled by two tunable parameters, the area of the air gun and the initial air gun pressure. Increasing either of these parameters will result in a faster rate of mass flow out of the air gun.

The expansion rate of the bubble is limited by the inertia of the water that must be accelerated to accommodate bubble growth, which increases with R. If the mass in the bubble increases rapidly with negligible changes in volume, p_b will increase. This will cause the small bubble to expand quickly and generate a high amplitude peak acoustic pressure with a short rise time. As shown in Figure 8, increasing the mass flow rate results in a greater amplitude peak pressure, a shorter rise time and a steeper slope.

The slope of the initial peak is used as a proxy for environmental impact (Chelminski et al., 0; Ronen and Chelminski, 2018). A shallower slope will produce fewer high frequency acoustic waves. The slope can be reduced by decreasing the air gun firing pressure. An air

gun with the parameters listed in Table 1 operated at 2000 psi will have a peak pressure of 4.3 bar m and a slope 2.6 bar m/ms compared to a peak pressure of 2.9 bar m and a slope

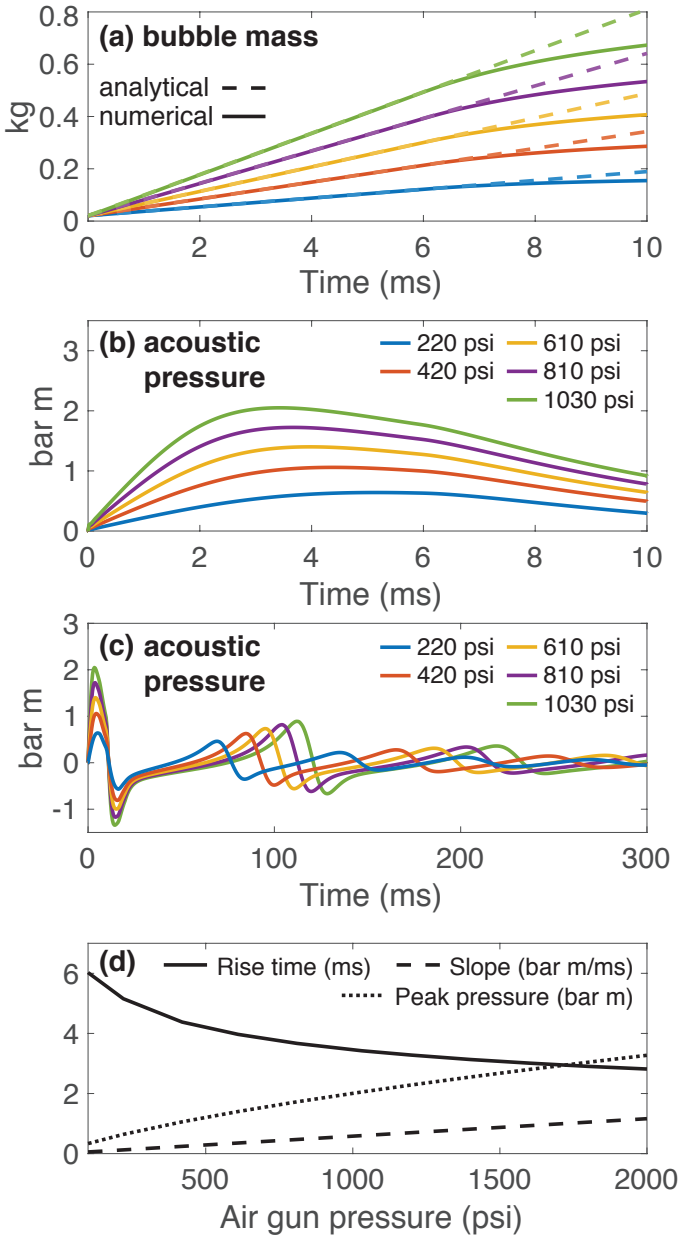

Figure 8: (a) **Bubble mass for a range of initial air gun pressures computed numerical using the 1D air gun model (solid) and approximate analytical solution valid prior to reflections from the end of the air gun (equation 35, dashed). (b) Acoustic pressure for a range of initial air gun pressures and (c) extended time series of acoustic pressure shown in (b).**(d) Rise time, slope and peak amplitude of first peak in source signature as a function of initial air gun pressure. Decreasing the initial air gun pressure results in a longer rise time, shallower slope and lower peak acoustic pressure.

of 1.3 bar m/ms when operated at 1000 psi. **Note that reducing the air gun pressure will reduce the amount of mass ejected from the air gun and hence reduce the bubble oscillation period.**.

The ambient pressure depends upon the depth of the air gun, $p_\infty = p_{\text{atm}} + \rho_\infty g D$. Increasing the depth of the air gun increases p_∞, which acts to prevent the expansion of the bubble resulting in a slower rise time, shallower slope and lower peak pressure. However, changes in p_∞ with depth (from 22 psi at 5 m depth to 50 psi at 25 m depth) are much smaller than the air gun pressure (2000 psi) **and therefore** the effect of depth on the initial peak of the source signature is **small** for conventional air gun operating depths (Figure 9).

For longer air guns ($L \gtrsim 0.8$ m) the rise time, slope, and peak amplitude of the initial peak do not depend upon the length of the air gun (Figure 10). This is because the peak amplitude is reached before the rarefaction wave that is reflected from the back wall propagates back to the port at $t \approx 2L/c_0$. The mass flow out of the air gun is the same for all gun lengths and hence the rising side of initial peak is the same. However, the decay following the peak does depend upon the length, with longer air guns continuing to eject mass at a high rate for longer, causing a slower decay and hence broader pulses. **For shorter air guns ($L \lesssim 0.8$ m) the reflected depressurization wave returns to the port before the peak amplitude is reached. This causes the pressure at the port, and hence the mass flow out of the port, to decrease, resulting in a lower peak amplitude and shorter rise time. This effect cannot be captured by a lumped parameter model and hence**

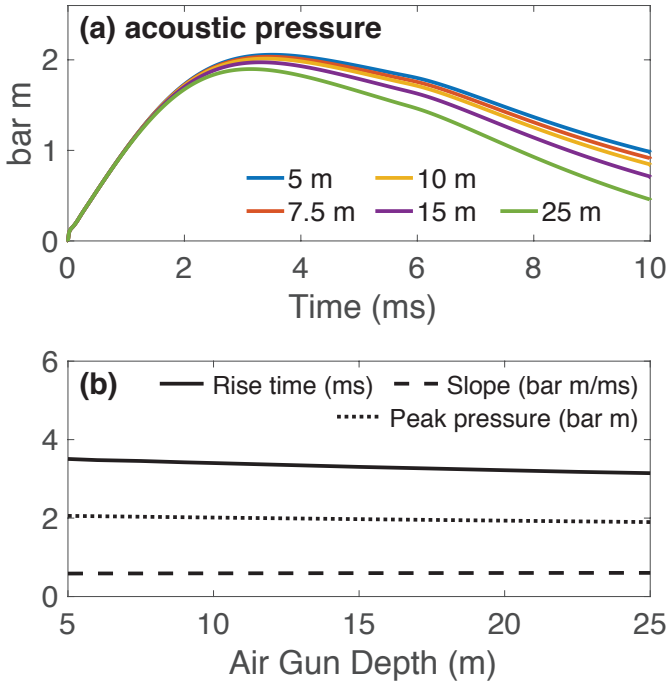

Figure 9: Acoustic pressure for a range of air gun depths. The air gun is pressurized to 1020 psi. **The slope is essentially independent of air gun depth while the rise time and peak pressure decrease slightly with increasing depth.**

the 1D model can provide new insights.

Bubble Oscillations

The low frequency limit of a seismic air gun signal is controlled by the bubble oscillations. There has been extensive work on modeling bubble dynamics (see Brennen (1995) and the references therein). The early work that proved most applicable to seismic air gun studies was done by Rayleigh (1917) who demonstrated that the period of bubble oscillations was proportional to the equilibrium radius of the bubble. A larger bubble will, all other things equal, oscillate slower. In conjunction with studies of the time interval between underwater explosion bubble oscillations (Willis, 1941; Cole, 1948), this early work formed the basis for the well-known Rayleigh-Willis equation, which is commonly used in the marine seismic exploration community (Hegna and Parkes, 2011; Barker and Landrø, 2013; Watson et al., 2016):

$$f = k\frac{(1 + D/10)^{5/6}}{(p_0 V_a)^{1/3}}, \tag{36}$$

where f is the frequency of bubble oscillations, D is the depth of the air gun in meters, p_0 and V_a are the operating pressure and volume of the air gun, respec-

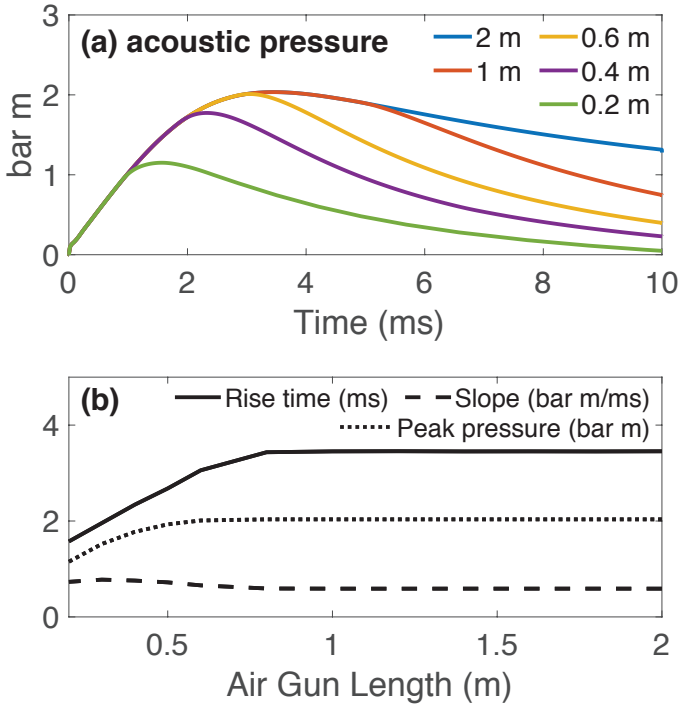

Figure 10: Acoustic pressure for a range of air gun lengths. The air gun is pressurized to 1020 psi **and fired at a depth of 7.5 m. The rise time, slope and peak acoustic pressure are independent of air gun length for long guns but depend upon the gun length for short guns.**

tively, and k is an empirical constant that depends upon the water properties, such as temperature and salinity, and the proportion of mass ejected from the gun. The lower the frequency of bubble oscillations, the more energy excited at geophysically useful low frequencies.

The depth dependency **arises because the ambient pressure, p_∞, increases with depth. At greater depths the equilibrium radius of the bubble is smaller, which means that the bubble period is shorter.** The pressure and volume dependency are both related to **the amount of mass discharged in the water**. **An air gun at higher pressure or with larger volume** is able to discharge more mass into the water forming a larger bubble that will oscillate slower **(Rayleigh, 1917).**

In summary, decreasing the operating pressure results in a reduced peak amplitude and slope, an increased rise time and, if the air gun volume is kept constant, a reduced bubble oscillation period. The initial peak is only weakly sensitive to the air gun depth. A greater depth results in slightly reduced peak amplitude, rise time, and slope. The depth does influence the bubble oscillation period with a deeper gun having a shorter period. For short guns, the initial peak depends upon the gun length. A shorter gun will have a smaller peak amplitude, slope, and rise time, while for longer guns, the initial peak is independent of the gun length. The bubble period depends upon the gun volume with a larger gun having a longer bubble oscillation period.

MODEL VALIDATION AGAINST FIELD DATA

Field Data

We compare our simulations to field data in order to validate our model, both via qualitative comparison to how changes in various operating/design parameters change the acoustic pressure, and actual quantitative comparisons. The simulations display the same general trends as the data: the rise time decreases with increasing pressure while the peak pressure and slope increase. The rise

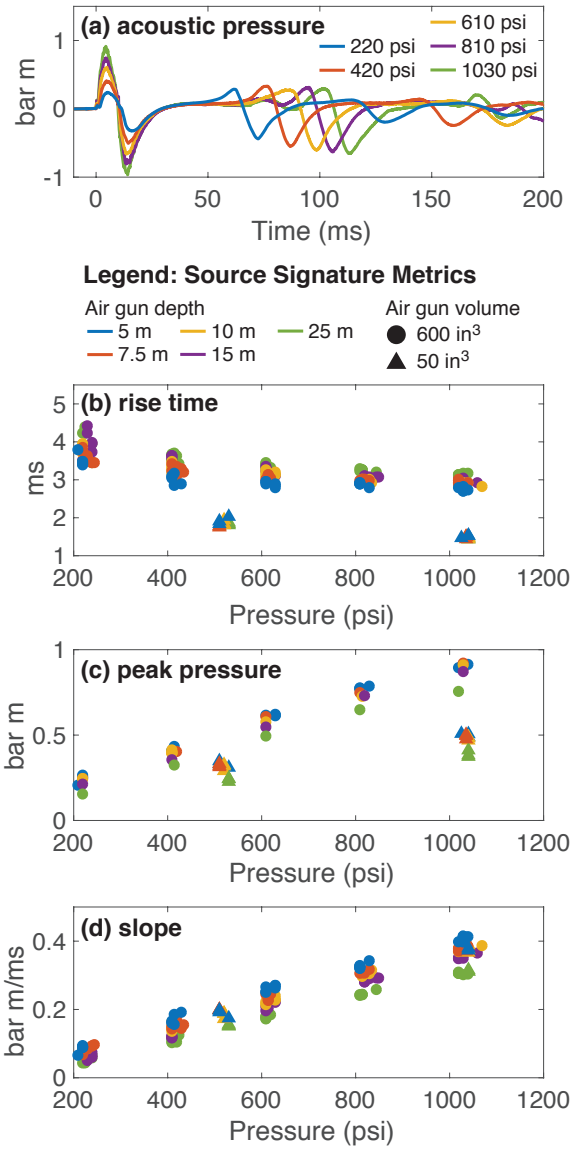

Figure 11: **Field data showing (a) acoustic pressure time series for a range of firing pressure and (b) rise time, (c) peak pressure and (d) slope of initial peak. The rise time decreases with increasing air gun pressure while the peak pressure and slope increase, which are the same trends seen in the simulations (Figure 8).**

time and peak pressure depend upon the gun length whereas the slope is independent of length. Gun depth, an important control on the bubble oscillation period, has a minor effect on the initial peak. Our initial simulations overpredicted the peak amplitude and bubble oscillation period; however, after parameter tuning and the inclusion of additional processes a good fit was obtained.

Field tests of a prototype air gun were carried out in Lake Seneca, **New York** (Chelminski et al., 0; Ronen and Chelminski, 2018). **Two different volume air guns, 50 in^3 and 600 in^3**, were fired at a range of pressures (220 - 1030 psi) and depths (5 - 25 m). **The gun lengths were 48 in (1.2 m) and 4 in (0.1 m), respectively. Both guns had a** cross-sectional area of 12.5 in^2 and a port area of 12 in^2 **with the ports located at the end of the gun**. Data were recorded by an array of 24 hydrophones suspended vertically below the air gun. **Here, we examine data from the nearest hydrophone, 75 m below the source.** The hydrophones recorded at 32 kHz, providing high resolution data **with which** to examine the initial peak of the source signature (Figure 11).

Comparing Field Data and Simulations

The simulations and field data **are qualitatively similar** (Figure 12), **with waveforms characterized by an initial peak with a fast rise and slower decay followed by**

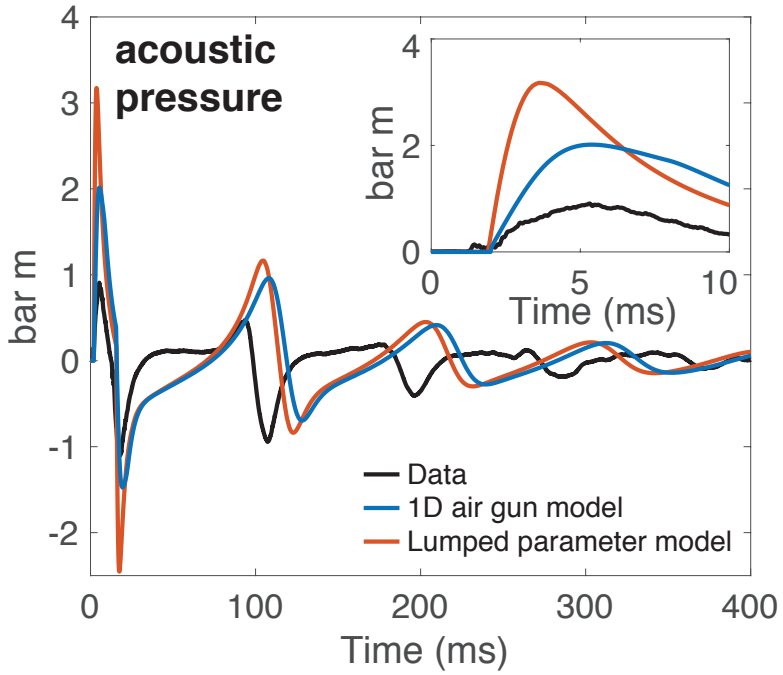

Figure 12: **Acoustic pressure time series showing field data (black), 1D air gun model (blue), and lumped parameter model (red). Inset focuses on the initial peak. The** 600 **in^3 air gun was fired at a depth of 10 m and pressure of 1030 psi. Other parameters are listed in Table 1.**

an oscillating coda. The peak acoustic pressure amplitude is reached within several milliseconds of the port opening and occurs before the end of discharge.

The trends displayed by the three metrics considered in this study, namely, peak pressure, rise time, and slope, are similar between the simulations and the data. The **amplitude and slope** of the initial peak increase with air gun pressure while the rise time decreases **(Figure 8)**. The initial peak is relatively insensitive to the depth of the air gun with a noticeably reduced peak amplitude only visible at 25 m depth (Figure 9). **The rise time and peak amplitude are proportional to the length of the gun while the slope is essentially independent (Figure 10).**

Quantitatively, however, there are differences between the data and simulations. The peak acoustic pressure recorded in the data is approximately **two** times smaller than in the simulations **of the 1D air gun model and three times smaller than the lumped parameter model**. **The rise times observed in the data are longer than in the simulations and the slope is smaller. The oscillation period of the simulations is longer than in the data.**

We consider three possible processes that may explain the discrepancies between data and simulations: (1) turbulence in the water, (2) port throttling, and (3) a seed bubble. We initially consider each hypothesized process individually, but later find that a combination of processes is required to match the data.

Turbulence in Water

Mechanical energy dissipation, for instance due to turbulence in the water, is parameterized by the $\alpha\dot{R}$ term in the bubble equation of motion (equation 8). Previous authors have assumed a constant value of α (Langhammer and Landrø, 1996; Watson et al., 2017a). Larger values of α increase the amount of mechanical energy dissipation. Langhammer and Landrø (1996) used $\alpha = 4$ m/s to model the signature recorded from a small air gun fired in a laboratory while Watson et al. (2017a) required $\alpha = 0.8$ m/s to match signatures of a 400 in^3 air gun from the commercial software *Nucleus*.

Increasing α causes the peak amplitude to decrease, but not by the factor of two required to match the data. Increasing α from 0 to 2 m/s causes the peak amplitude to decrease from 2.1 bar m to 2.0 bar m, which is still significantly higher than the peak data amplitude of 0.9 bar m (Figure 13). Increasing α further does continue to decrease the peak amplitude. For example, when $\alpha = 10$ m/s the peak amplitude is reduced to 1.8 bar m. However, this slight decrease in the peak amplitude is achieved at the expense of introducing substantial dissipation such that, for $\alpha = 10$ m/s, the bubble oscillations are entirely damped out, which is inconsistent with the observations.

An alternative parameterization, motivated by the nonlinearity of turbulence, is $\alpha = \beta|\dot{R}|$ for some positive, dimensionless constant β. With this parameterization, the amplitude of the damping varies as the bubble oscillates. Dissipation is greatest during the initial stages of bubble expansion when $\dot{R}$ is large (Figure 13) and, depending on the value of β, can be substantially larger

than the constant values of α used by Langhammer and Landrø (1996) and Watson et al. (2017a).

The nonlinear parameterization of the dissipation term can reduce the peak amplitude, from 2.1 bar m for $\alpha = 0$ to 1.7 bar m for $\alpha = |\dot{R}|$ and 1.2 bar m for $\alpha = 5|\dot{R}|$, which is approaching the peak amplitude of the data, 0.9 bar m. However, just like for the constant α parameterization, increasing β to match the peak amplitude causes the bubble oscillations to be damped out. Therefore, while the parameterization of the mechanical energy dissipation term does matter, this process alone is not sufficient to explain to amplitude discrepancy between the data and simulations without excessively damping the bubble oscillations.

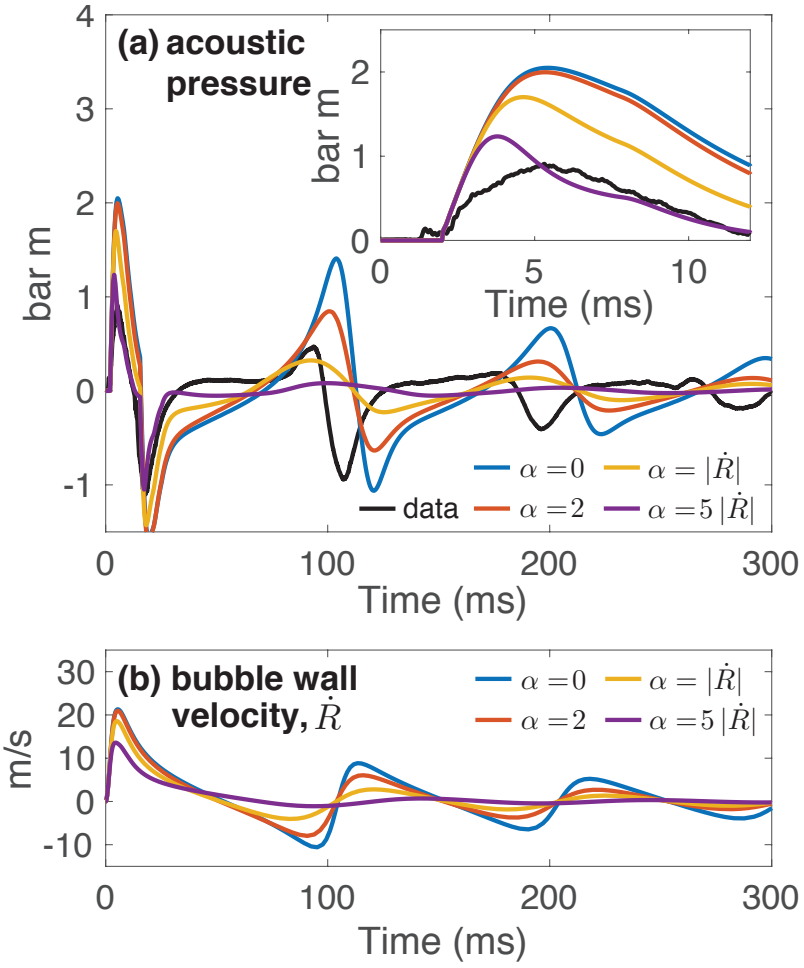

Figure 13: **(a) Simulated acoustic pressure for different parameterizations of the dissipation term, $\alpha\dot{R}$, in equation 8. Inset focuses on the initial peak. The 600 in^3 air gun was fired at a depth of 10 m and pressure of 1030 psi. (b) Bubble wall velocity, $\dot{R}$, corresponding to the simulations shown in (a). Increasing the amount of mechanical energy dissipation can cause the peak amplitude of the simulations to decrease to match the data, but not without damping out the bubble oscillations.**

Port Throttling

The simulations predict a bubble period that is slightly longer than that of the data (e.g., Figure 12). The period of the bubble oscillations is related to the mass of air in the bubble (equation 36), suggesting that more mass is ejected from the air gun in our simulations than in the data. This is plausible because our simulations neglect the finite port opening time and assume that the port area is equal to the cross-sectional area of the gun. The modeling work of Watson et al. (2016) required a reduced port area in order to match the period of the data. Another process that might reduce velocity at the port is energy dissipation and pressure drop from turbulent eddies and possibly even shocks formed as compressible gas flows through internal constrictions or the port.

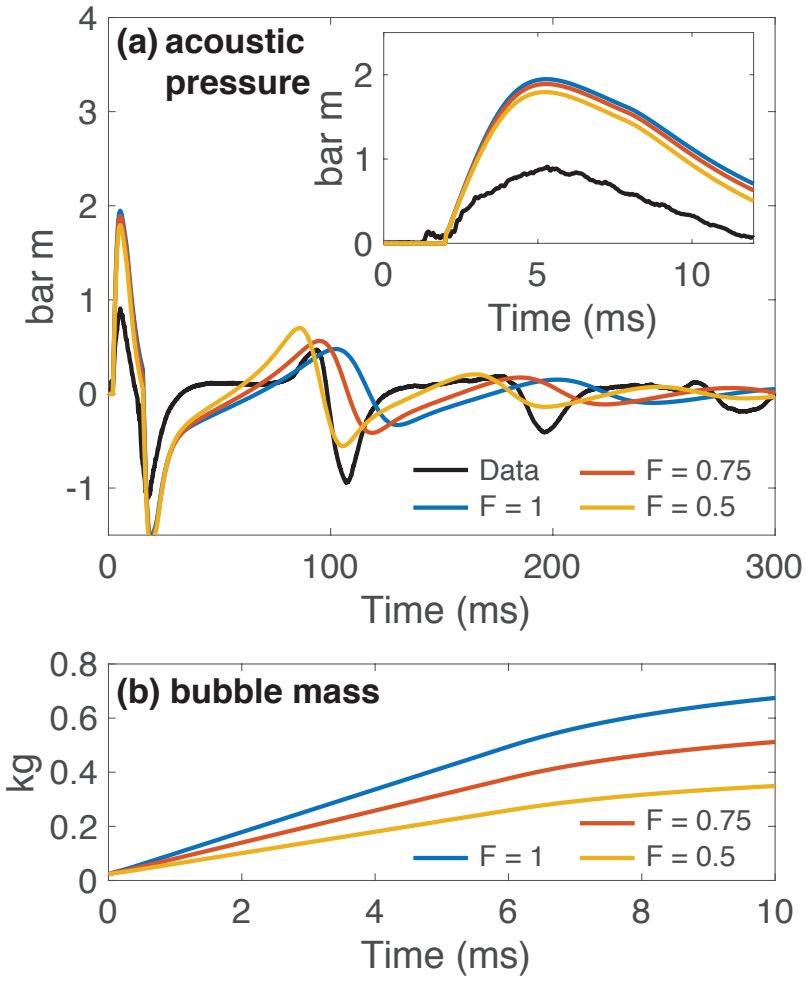

Figure 14: **(a) Simulated acoustic pressure for a range of values of F, the mass flow reduction factor (equation 37). Inset focuses on the initial peak. The** 600 **in^3 air gun was fired at a pressure of 1030 psi and depth of 10 m. (b) Bubble mass corresponding to the simulations shown in (a).**

As a proxy for the processes causing reduced mass flow rate, we modify equation 25 to

$$\frac{dm_b}{dt} = Fv(L)\rho(L)A, \tag{37}$$

where $F \in [0, 1]$ is the mass flow reduction factor.

Reducing the mass flow out of the air gun does reduce the bubble period but does little to reduce the peak amplitude. Decreasing the mass flow rate to 50% of the original flow rate only reduces the peak amplitude by 10%, from 2.0 bar m to 1.8 bar m. Decreasing the mass flow to even smaller values results in far too little mass entering the bubble and unrealistically small bubbles that oscillate far quicker than seen in the data. Therefore, the discrepancy between the amplitude of the data and simulations cannot be explained solely by reducing the mass flow out of the gun.

Seed Bubble

A third process that could account for the discrepancy between data and simulations is the initial bubble volume. The bubble dynamics governing equations that have been proposed in the literature, including the widely used Gilmore equation (Gilmore, 1952; Ziolkowski, 1970; Li et al., 2010; de Graaf et al., 2014b) and the modified Herring equation used here (equation 8; Herring, 1941; Cole, 1948; Vokurka, 1986), take the form of $\ddot{R} = 1/R \times [\cdots]$ and become singular when $R = 0$. Therefore, the simulations are initialized with some choice of non zero bubble radius.

The **most** common choice, first proposed by Ziolkowski (1970) **as the simplest possible initial condition**, is to initialize the bubble radius such that the volume of the bubble is equal to the volume of the air gun:

$$R_0 = \left(\frac{3V_a}{4\pi}\right)^{\frac{1}{3}}, \tag{38}$$

where V_a is the volume of the air gun and R_0 is the initial bubble volume. **The initial bubble volume can be viewed as the volume of a seed bubble that is released prior to the main discharge of air.**

The choice of the initial bubble volume, for typical gun volumes, is not significant when the focus is on bubble oscillations. This is because the frequency of the bubble oscillations is controlled by the equilibrium bubble radius (Rayleigh, 1917; Willis, 1941), which is related to the bubble mass and ambient pressure. The amount of mass in the initial bubble is small ($\sim$0.01 kg for a 300 in^3 initial bubble volume at a depth of 7.5 m **or $\sim$0.03 kg for a 1,000 in^3 volume**) compared to the amount of mass ejected from the air gun into the water ($\sim$1 kg for the air gun parameters described above). Therefore, the exact choice of initial bubble volume does not significantly influence the **period of bubble oscillations, provided the initial bubble volume is much smaller than the equilibrium bubble volume (for reference, the equilibrium bubble radius for a typical air gun is $\sim$0.5 m, which corresponds to a volume of $\sim$32,000 in^3).**

The choice of initial bubble volume, however, is extremely important when considering the initial peak in the source signature (Figure 15). A large initial bubble buffers the effect

of mass flow from the air gun into the bubble. A greater amount of mass addition to the bubble is required in order to appreciably increase the bubble pressure and drive expansion. Therefore, the bubble expands slower resulting in a longer rise time, lower peak amplitude and lower slope. Conversely, a small bubble will expand rapidly and correspondingly will generate a greater amplitude pressure perturbation with a shorter rise time and higher slope (Figure 15). **For an initial bubble volume of 600 in^3 the peak pressure is 2.0 bar m and the rise time is 3.4 ms compared to 1.6 bar m and 6.2 ms for an initial bubble volume of 2500 in^3.**

A nonzero initial bubble volume is physically plausible due to air leaking from the air gun prior to the specified firing time. In fact, there is a small precursor peak in the data that could be due to air leaking from the gun (Figure 16). This air could form into a seed bubble that buffers the initial bubble expansion and reduces the amplitude of the initial peak.

The sensitivity of the solution to the initial bubble radius suggests that in order to reduce the peak amplitude and slope of the initial peak, a seed bubble could be purposely formed by releasing a small amount of air before the

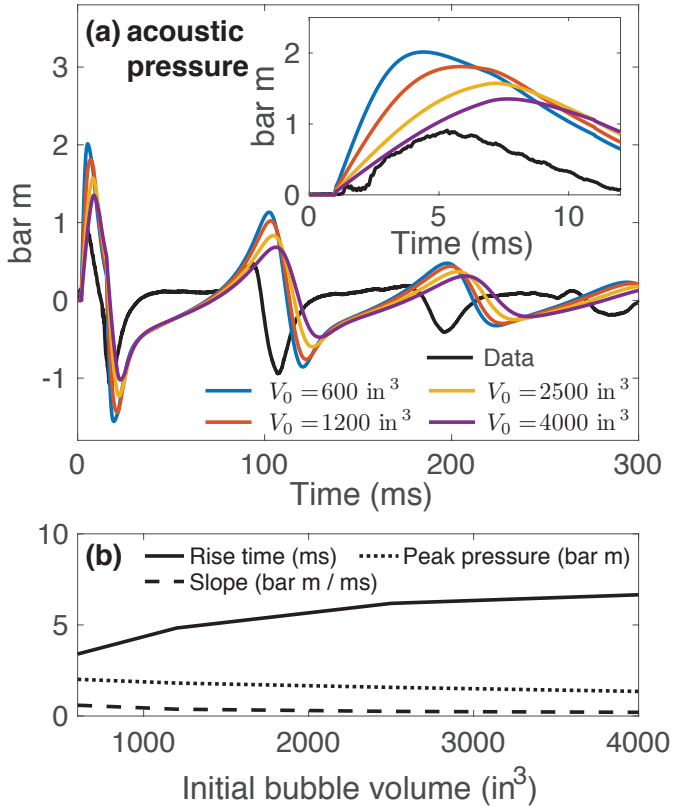

Figure 15: **(a) Simulated acoustic pressure for a range of initial bubble volumes. Inset focuses on initial peak. The 600 in^3 air gun was at a pressure of 1030 psi and depth of 10 m. (b) Rise time, slope and peak pressure as a function of initial bubble volume.**

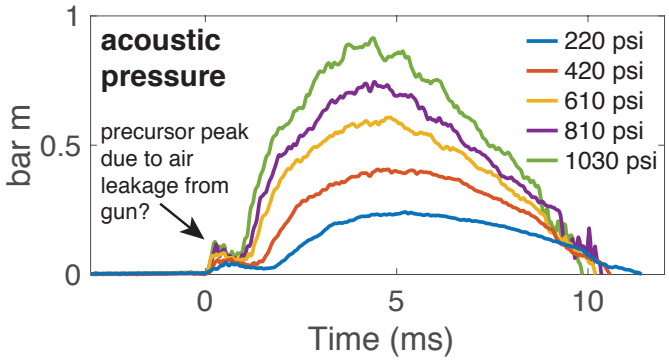

Figure 16: **Field data showing acoustic pressure time series of a range of firing pressures. Precursor peak is present in all shots and scales with firing pressure.**

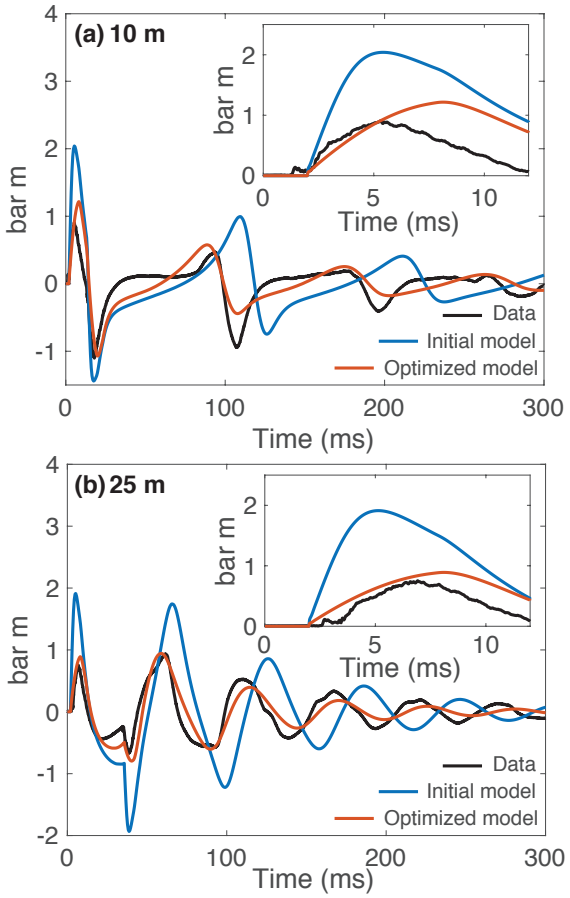

Figure 17: **Acoustic pressure time series showing field data (black), initial model (blue) and optimized model (red) for a** 600 **in**^{3} **seismic air gun with a pressure of 1030 psi discharged at a depth of (a) 10 m and (b) 25 m. The tuning parameters used in the corrected model are for (a)** $\alpha = 0.8|\dot{R}|$, $F = 0.45$ **and** $V_0 = 3000$ **in**^{3} **and for (b)** $\alpha = 0.8|\dot{R}|$, $F = 0.3$ **and** $V_0 = 5000$ **in**^{3}

majority of discharge. This idea is similar to the GI gun that discharges air in two stages in order to stabilize the bubble and minimize the amplitude of bubble oscillations (Landrø, 1992).

Combination of Processes

In the previous sections we demonstrated how the discrepancy between the data and the simulations cannot be resolved by any of the three processes proposed in isolation. However, by combining multiple processes we are able to achieve a much better fit to the data (Figure 17). Here, parameters were tuned by hand. Future work should more rigorously explore possible parameter values using a formal inversion procedure, investigate interdependencies between the different parameters, and, of course, introduce more rigorous descriptions of the proposed processes considered as part of this comparison exercise.

Overall, though, we have demonstrated that the 1D model presented here is better able to explain the data than the lumped parameter model. The 1D model has a smaller peak amplitude and peak-to-bubble ratio (ratio between the amplitudes of the first and second peaks). It also correctly explains the dependence of the initial peak on the gun length.

CONCLUSION

Seismic air guns are the predominant source used in marine seismic exploration surveys. There is significant interest in understanding the source signature of an air gun in order to minimize the high frequency components. Lumped parameter models are widely used in modeling seismic air gun dynamics and have proven to be extremely successful at predicting the bubble period and coda of the source signature. However, not accounting for spatially variable depressurization within the air gun firing chamber can lead to a significant over prediction of the amplitude, slope and shape of the initial peak of the source signature. Here, we have demonstrated the utility of a quasi-one-dimensional model of an air gun that describes gas dynamics within the firing chamber. **This model and the associated analytical expressions presented here provide insight into the controls on the initial peak of an air gun source signature.**

The initial peak in an air gun source signature is strongly dependent upon the air gun firing pressure. A lower pressure results in a longer rise time, reduced peak amplitude and shallower slope, and hence reduces the amplitude of environmentally damaging high frequencies. The initial peak is only weakly sensitive to the depth. For long guns ($\gtrsim 0.8$ m) the initial peak is independent of the gun length because the peak pressure is reached before the rarefaction wave reflects from the back wall and propagates back to the port.

The dual goals of increasing the amplitude of the low frequency acoustic waves and decreasing the high frequencies are incongruous, **at least for fixed gun volume**. The low frequency content increases when more mass is discharged into the water forming a larger bubble that oscillates slower. The slope, which is a proxy for the amplitude of high frequency acoustic waves, decreases when the initial air gun pressure is decreased. However, decreasing the initial air gun pressure reduces the amount of mass that is discharged and hence will result in decreased amplitude at low frequencies. Therefore, there is no universally optimal air gun design. Instead, the optimal operating pressure and gun size depend upon the specific objectives **and environmental considerations** of each survey.

The simulations and data presented here are qualitatively similar but the simulations require consideration of additional processes in order to match the data. The peak amplitudes predicted by the simulations, without the additional processes, are 2-3 times larger than in the data. We speculate on three potential mechanisms: (1) mechanical energy dissipation due to turbulence in the water, (2) a reduced mass flow out of the gun due to port constriction, and (3) a seed bubble buffering initial expansion. Mechanical energy dissipation is unable to sufficiently reduce the peak amplitude without damping out the bubble oscillations. Decreasing the mass flow rate out of the port only causes a slight decrease in the peak amplitude but significantly decreases in the bubble period. The presence of a seed bubble in the water buffers the initial bubble expansion and can result in significant decreases in the peak amplitude, such that the peak amplitude of the simulations approaches that of the data. However, none of these mechanisms alone can explain all discrepancies between the simulations and data. Instead, a combination of the different effects is required. We do caution that the parameterizations of the additional processes are relatively ad hoc and future work should focus on describing them more rigorously.

The work presented here fills an important niche between commonly used

lumped parameter models and more recent work using high-fidelity but computationally expensive CFD simulations. Our main focus was to systematically investigate how different physics and parameters influence the source signature of an air gun, specifically focusing on the initial peak that is most responsible for the environmentally damaging high frequency radiation. The quasi-one-dimensional approximation is a simplified representation of an air gun. Nonetheless, it provides useful insight into the controls on the source signature of an air gun and is able to well explain the trends seen in the data. Future work should focus on more accurately treating the port area, accounting for the turbulence in the water and a turbulent pressure drop due to the compressible flow of air through the constriction of the port, and further exploring the idea of a seed bubble released before the main discharge of air.

ACKNOWLEDGMENTS

Data is provided courtesy of Chelminski Technology and Shearwater Geophysical. We thank Shuki Ronen for many useful discussions about seismic air guns and Martin Almquist, Ossian O'Reilly and Ken Mattsson for assistance with the numerics. This work was supported by the Swedish Foundation for International Cooperation in Research and Higher Education (STINT:IB2014-5910) and the Stanford Exploration Project. The code is hosted online at github.com.

APPENDIX A: BUBBLE MODELS

There are a plethora of bubble models in the seismic air gun literature. The various models all consider a spherical bubble oscillating in a fluid and can be derived by evaluating conservation of momentum of the fluid on the bubble wall (Kirkwood and Bethe, 1942; Gilmore, 1952). Different models arise when various powers of the ratio of the bubble wall velocity, $\dot{R}$ to the speed of sound in the fluid, c, are included.

The Rayleigh equation (Rayleigh, 1917) is the zero-order approximation and considers a bubble oscillating in an incompressible fluid with an infinite speed of sound:

$$\ddot{R}R + \frac{3}{2}\dot{R}^2 = \frac{p - p_\infty}{\rho_\infty}. \tag{A-1}$$

The terms on the left side describe the inertia of the water while the right side denotes the pressure difference across the bubble wall. The Rayleigh equation does not allow for acoustic damping and hence, in the absence of any other damping mechanisms, predicts that the bubble will oscillate indefinitely. Therefore, it is rarely used to model seismic air gun dynamics.

The first-order approximation of fluid compressibility gives rise to the Herring equation (Herring, 1941):

$$\ddot{R}R\left(1 - 2\frac{\dot{R}}{c_\infty}\right) + \frac{3}{2}\dot{R}^2\left(1 - \frac{4}{3}\frac{\dot{R}}{c_\infty}\right) = \frac{p - p_\infty}{\rho_\infty} + \frac{R}{c_\infty}\frac{\dot{p}}{\rho_\infty}\left(1 - \frac{\dot{R}}{c_\infty}\right), \tag{A-2}$$

where the last term accounts for damping from acoustic radiation.

The modified Herring equation, which is used in this work, is obtained by neglecting the $\dot{R}/c_\infty$ terms in the Herring equation (Vokurka, 1986). This is justified by laboratory studies (Langhammer and Landrø, 1996; de Graaf et al., 2014a) and numerical simulations (Li et al., 2010) which show that the bubble wall velocity, $\dot{R} \approx 50$ m/s, is small compared to the speed of sound in water, $c_\infty \approx 1500$ m/s. The modified Herring equation is given by:

$$\ddot{R}R + \frac{3}{2}\dot{R}^2 = \frac{p - p_\infty}{\rho_\infty} + \frac{R}{c_\infty}\frac{\dot{p}}{\rho_\infty}, \tag{A-3}$$

and is similar to the Rayleigh equation (equation A-1). The additional term on the right side is a correction for compressibility that allows for energy loss through acoustic radiation.

The Gilmore equation (Gilmore, 1952) includes second-order compressibility effects and allows the speed of sound in the fluid to vary with pressure. The Gilmore equation is the most commonly used equation in the seismic air gun literature (e.g., Landrø et al., 1994; Laws et al., 1998; Li et al., 2010; de Graaf et al., 2014b). It was originally developed for underwater explosions (Gilmore, 1952) before being applied to seismic air guns (Ziolkowski, 1970) and is given by:

$$\ddot{R}R\left(1 - \frac{\dot{R}}{c}\right) + \frac{3}{2}\dot{R}^2\left(1 - \frac{\dot{R}}{3c}\right) = H\left(1 + \frac{\dot{R}}{c}\right) + \frac{R\dot{H}}{c}\left(1 - \frac{\dot{R}}{c}\right), \tag{A-4}$$

where H is the enthalpy difference and c is the local speed of sound:

$$H = n\left(\frac{p_\infty + B}{(n-1)\rho}\right)\left[\left(\frac{p+B}{p_\infty + B}\right)^{(n-1)/n} - 1\right], \tag{A-5}$$

$$c = c_\infty\left(\frac{p+B}{p_\infty + B}\right)^{(n-1)/2n}, \tag{A-6}$$

where $B = 3000$ atm and $n = 7$ are constants from the Tait equation of state (Gilmore, 1952; de Graaf et al., 2014b).

For all models, the pressure inside the bubble is calculated by the ideal gas equation of state:

$$p_b = \frac{m_b Q T_b}{V_b}. \tag{A-7}$$

For a closed bubble with no mass flow in or out, the evolution of temperature inside the bubble is given by

$$\frac{dT_b}{dt} = \frac{1}{c_v m_b}\left[-4\pi R^2 M\kappa(T_b - T_\infty) - p_b\frac{dV_b}{dt}\right]. \tag{A-8}$$

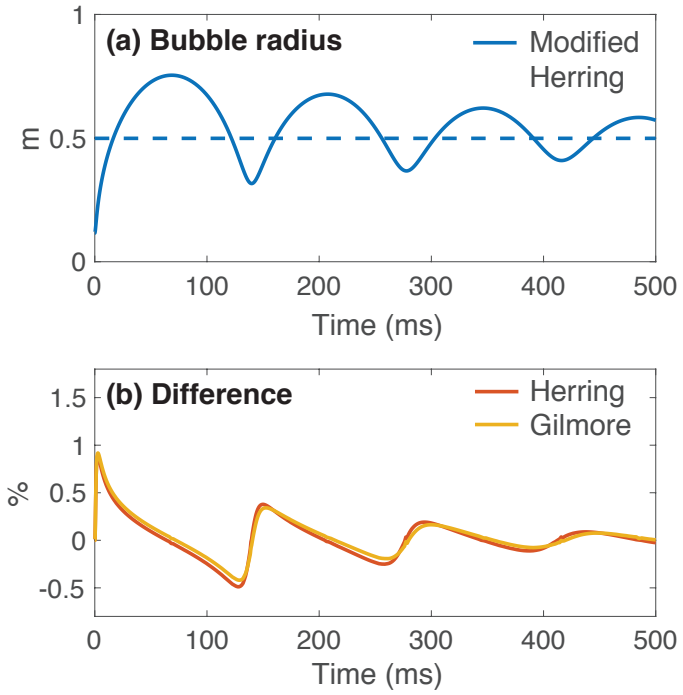

Figure A-1: (a) Bubble radius predicted by the modified Herring equation (equation A-3) for a bubble of air with initial volume of 400 in^3 and pressure of 2000 psi at a depth of 7 m accounting for conductive heat loss (equation A-8). Horizontal dashed line indicates the equilibrium bubble radius. (b) Percentage difference between the modified Herring equation and the Herring (equation A-2) and Gilmore (equation A-4) equations. **All models are initialized with the same values as for the modified Herring equation.**

Numerical simulations of bubble dynamics for the parameter space of interest for seismic air guns show no appreciable difference between the solutions of the Herring, modified Herring, or Gilmore equation (Figure A-1). This is because the bubble wall velocity is small compared to the speed of sound in water, as discussed above, and hence higher order compressibility corrections, such as those included in the Gilmore equation, can be neglected.

This is in agreement with the work of Vokurka (1986) who compared the Herring, modified Herring and Gilmore equation. Vokurka (1986) defined A as the ratio of the maximum bubble radius to equilibrium bubble radius and showed that the radius predicted by the Herring and modified Herring equation are within 5% of that calculated using Gilmore equation for values of A up to 4.5 with the difference between the models decreasing as $A \rightarrow 1$. For the parameter space of interest for seismic air guns $A \approx 1.5$, as shown in Figure A-1. Hence, we argue that the modified Herring equation should be used in lumped parameter models of air gun bubbles. It produces essentially identical results to the commonly used Gilmore equation but is computationally simpler.

APPENDIX B: NUMERICAL SCHEME

This appendix describes the space discretization of the air gun and its coupling to the bubble. The space discretization is constructed with finite differences using the summation-by-parts (SBP) framework with the boundary and coupling conditions imposed using the simultaneous approximation term (SAT) penalty technique (Svärd and Nordström, 2014). The coupled partial differential equation (PDE) air gun and ordinary differential equation (ODE) bubble models are discretized into a pure ODE system. The time integration of this ODE system performed using an embedded Runge-Kutta method. Here, we first describe the Euler equations with boundary and coupling conditions in a form suitable for discretization and then discuss the operators used in the discretization and how they are applied in the scheme.

Continuous Formulation

The Euler equations for the air gun written in conservative system form are

$$\begin{cases} \dfrac{\partial q}{\partial t} + \dfrac{\partial f(q)}{\partial x} = 0, & 0 < x < L, \quad 0 \leq t \leq T \\ q = q_0, & t = 0 \end{cases} \tag{A-9}$$

where

$$q = \begin{bmatrix} q_1 \\ q_2 \\ q_3 \end{bmatrix} = \begin{bmatrix} \rho \\ \rho v \\ e \end{bmatrix}, \quad f(q) = \begin{bmatrix} \rho v \\ \rho v^2 + p \\ (e+p)v \end{bmatrix}, \tag{A-10}$$

with the equation of state

$$p = (\gamma - 1)(e - \frac{1}{2}\rho v^2). \tag{A-11}$$

The flux function, $f(q)$, and the pressure, p, can be rewritten in terms of the components of q:

$$f(q) = \begin{bmatrix} q_1 \\ q_2^2/q_1 + p \\ (q_3 + p)q_2/q_1 \end{bmatrix}, \tag{A-12}$$

$$p = (\gamma - 1)(q_3 - \frac{1}{2}q_2^2/q_1). \tag{A-13}$$

The boundary conditions for the PDE considered in this work are a wall boundary condition at the back wall of the firing chamber and a pressure boundary condition at the air gun port,

$$\begin{aligned} v &= 0, & x &= 0, \\ p &= p_b(t), & x &= L. \end{aligned} \tag{A-14}$$

Written in quasi-linear form these boundary conditions take the form:

$$\begin{aligned} &L_{\text{bw}} q = 0, && L_{\text{bw}} = \begin{bmatrix} 0 & 1 & 0 \end{bmatrix}, && x = 0, \\ &L_{\text{p}}(q) q = p_a(t), && L_{\text{p}} = (\gamma - 1)\begin{bmatrix} 0 & -\frac{1}{2}q_2/q_1 & 1 \end{bmatrix}, && x = L. \end{aligned} \tag{A-15}$$

For the purpose of flux splitting and enforcing boundary conditions the flux function can also be written in quasi-linear form:

$$f(q) = A(q)q, \tag{A-16}$$

where

$$A = \begin{bmatrix} 0 & 1 & 0 \\ \frac{1}{2}(\gamma-3)u^2 & (3-\gamma)u & \gamma-1 \\ (\gamma-1)u^3 - \frac{\gamma e}{\rho}u & \frac{\gamma e}{\rho} - \frac{3}{2}(\gamma-1)u^2 & \gamma u \end{bmatrix}. \tag{A-17}$$

This matrix is diagonalized by

$$T = \begin{bmatrix} \sigma\rho & \rho & \rho \\ \sigma\rho u & \rho(u+c) & \rho(u-c) \\ \sigma\rho u^2/2 & e + (\gamma-1)(e-\rho u^2/2) + \rho u c & e + (\gamma-1)(e-\rho u^2/2) - \rho u c \end{bmatrix}, \tag{A-18}$$

where $\sigma = \sqrt{2(\gamma-1)}$ and $c^2 = \gamma p/\rho$, such that

$$T^{-1}AT = \Lambda = \begin{bmatrix} u & 0 & 0 \\ 0 & u+c & 0 \\ 0 & 0 & u-c \end{bmatrix}. \tag{A-19}$$

At the air gun back wall velocity is zero, $v = 0$, which can be expressed as:

$$L_{\text{bw}} q = 0, \quad L_{\text{bw}} = \begin{bmatrix} 0 & 1 & 0 \end{bmatrix} \tag{A-20}$$

At the air gun opening the number of boundary conditions will change depending on the flow velocity. With supersonic outflow no conditions are allowed at the opening. For subsonic outflow one boundary condition is required, continuity of pressure at the opening and in the bubble, $p(t, x_{\text{p}}) = p_a(t)$, which can be expressed as:

$$L_{\text{p}} q = p_a(t), \quad L_{\text{p}} = (\gamma-1)\begin{bmatrix} 0 & -\frac{1}{2}v & 1 \end{bmatrix} \tag{A-21}$$

For subsonic and supersonic flow into the air gun, more boundary conditions are needed. However since the port closes before this happens, these cases do not arise.

Discretization

SBP upwind operators

Upwind finite difference operators with the special boundary closures introduced in Mattsson (2017) are used for discretizing space derivatives in the scheme. The boundary closures of these operators are constructed so that they fulfill a summation-by-parts property which we use here to implement boundary and coupling conditions in a robust way.

The finite-difference operators approximate the first derivative of a grid function using skewed finite difference stencils. Given a grid with nodes $\{x_i\}_{i=1}^N$ and a grid function $\bar{u}_i = u(x_i)$ we have:

$$\frac{\partial u}{\partial x}(x_i) = (D_\pm u)_i + O(h^p). \tag{A-22}$$

Here D_+ and D_- both approximate the first derivative but have their stencils skewed in different directions.

Due to their special construction the operators can be written in the form:

$$D_\pm = H^{-1}\left(Q_\pm + \frac{1}{2}B\right), \tag{A-23}$$

where $H = H^\top$ defines an inner product and $B = -e_l e_l^\top + e_r e_r^\top$. Further, e_l and e_r are column vectors that pick out the first and last value of a grid function. For Q_+ and Q_- we have that $Q_+ + Q_-^\top = 0$ as well as that $Q_- Q_-^\top$ is positive definite.

The decomposition of $D_\pm$ into H, $Q_\pm$ and B ensures that the operators mimic the integration by parts property of the continuous derivative. By introducing the discrete inner product $(u, v)_H = u^\top H v$, and using the decomposition in (A-23) we can write:

$$(u, D_+ v)_H = (e_r^\top u)(e_r^\top v) - (e_l^\top u)(e_l^\top v) - (D_- u, v)_H, \tag{A-24}$$

which is the summation by parts property. This property enables a robust implementation of the boundary conditions using a penalty method. Finally, the property that $Q_+ + Q_+^\top \geq 0$, ensures that when these operators are used in a flux splitting scheme they introduce damping throughout the whole domain, including the boundaries.

Flux-splitting

Using a flux splitting together with summation-by-parts upwind finite difference operators allows for accurate artificial dissipation as well as a robust boundary condition treatment. Using flux splitting:

$$f_\pm = f(q) + (c + |v|)q, \tag{A-25}$$

and discretization the split form of (A-9) using the upwind operators leads to:

$$\frac{dq}{dt} + D_+ f_+(q) + D_- f_-(q) = 0. \tag{A-26}$$

Boundary conditions

Boundary conditions are imposed weakly using the simultaneous approximation term technique (Carpenter et al., 1994). Here we use the very general hyperbolic system treatment of Eriksson (2016). This provides a robust implementation for the boundary and coupling conditions.

The complete discretization of the PDE including boundary conditions is the system of ODEs:

$$\begin{aligned} \frac{dq}{dt} + D_+ f_+(q) + D_- f_-(q) = {} & H^{-1}\tau_{\text{bw}}(L_{\text{bw}} e_0^\top q - 0) \\ & + H^{-1}\tau_{\text{p}}(L_{\text{p}} e_L^\top q - p_a(t)), \end{aligned} \tag{A-27}$$

where τ_{bw} are τ_{p} are penalty parameters chosen to ensure stability, in this case:

$$\begin{aligned} \tau_{\text{bw}} &= |\Lambda_-|\,, \\ \tau_{\text{p}} &= |\Lambda_+|\,. \end{aligned} \tag{A-28}$$

Using standard techniques it is possible the show that this scheme for the frozen coefficient problem provides the same energy bounds as the continuous problem.

Summary of Numerical Scheme

Combining (A-27) with the ODE model of the bubble we now have discretization of the full problem as a system of ODEs. The discretization includes a small amount of artificial dissipation and implements boundary conditions on the air gun and the coupling conditions between the bubble and the air gun in a robust way.

Sensitivity to Spatial Discretization

The air gun is discretized with uniform grid spacing. The time scale of the transition from the initial conditions to the analytical sonic solution depends upon the grid spacing. The time scale decreases when the grid is refined (Figure A-2a) and in the limit that the grid spacing approaches zero the transition will occur instantaneously.

The acoustic pressure is relatively insensitive to the spatial discretization of the air gun as the initial transient has a negligible effect on bubble dynamics. The rise time, slope and

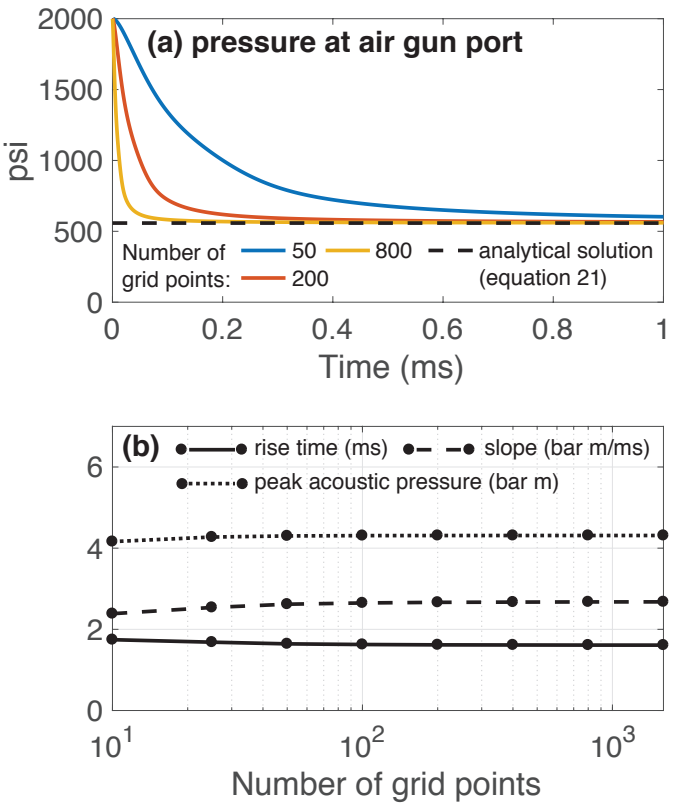

Figure A-2: Numerical resolution test of the sensitivity of the solution to the number of grid points used to discretize a 1 m long air gun. (a) Pressure at air gun port for 50, 200 and 800 grid points. The time scale of the transition from the initial conditions to the sonic solution depends upon the grid resolution. (b) Rise time, slope and peak acoustic pressure as a function of the number of grid points. These metrics of the initial acoustic pressure pulse are essentially independent of the number of grid points.

peak acoustic pressure change by less than 1% when the grid is refined from 100 to 1000 grid points (Figure A-2b). In this work we discretize the air gun chamber with 100 grid points per meter.

REFERENCES

Babu, V., 2014, Fundamentals of Gas Dynamics, 2nd ed.: John Wiley & Sons.

Barker, D., and M. Landrø, 2013, Estimation of bubble time period for air-gun clusters using potential isosurfaces: Geophysics, **78**, P1–P7.

Brennen, C. E., 1995, Cavitation and Bubble Dynamics: Oxford University Press.

Carpenter, M. H., D. Gottlieb, and S. Abarbanel, 1994, Time-stable boundary conditions for finite-difference schemes solving hyperbolic systems: methodology and application to high-order compact schemes: Journal of Computational Physics, **111**, 220–236.

Chapman, C. J., 2000, High Speed Flow: Cambridge University Press.

Chelminski, S., L. M. Watson, and S. Ronen, 0, Low frequency pneumatic seismic sources: Geophysical Prospecting.

Cole, R. H., 1948, Underwater explosions: Princeton University Press.

Coste, E., D. Gerez, H. Groenaas, J.-f. Hopperstad, O. P. Larsen, R. Laws, and S. Gould, 2014, Attenuated high-frequency emission from a new design of air-gun: 132–137.

de Graaf, K. L., P. A. Brandner, and I. Penesis, 2014a, Bubble dynamics of a seismic airgun: Experimental Thermal and Fluid Science, **55**, 228–238.

de Graaf, K. L., I. Penesis, and P. A. Brandner, 2014b, Modelling of seismic airgun bubble dynamics and pressure field using the Gilmore equation with additional damping factors: Ocean Engineering, **76**, 32–39.

Del Rey Fernández, D. C., J. E. Hicken, and D. W. Zingg, 2014, Review of summation-by-parts operators with simultaneous approximation terms for the numerical solution of partial differential equations: Computers and Fluids, **95**, 171–196.

Eriksson, S., 2016, A Dual Consistent Finite Difference Method with Narrow Stencil Second Derivative Operators: Journal of Scientific Computing.

Finneran, J. J., 2015, Noise-induced hearing loss in marine mammals : A review of temporary threshold shift studies from 1996 to 2015: Journal of Acoustical Society of America, **138**, 1702–1726.

Gerez, D., H. Groenaas, O. P. Larsen, M. Wolfstirn, and M. Padula, 2015, Controlling air-gun output to optimize seismic content while reducing unnecessary high-frequency emissions: SEG Technical Program Expanded Abstracts 2015, 154–158.

Gilmore, F. R., 1952, The Growth or Collapse of a Spherical Bubble in a Viscous Compressible Liquid: Technical report, Hydrodynamics Laboratory, California Institute of Technology.

Goldbogen, J. A., A. K. Stimpert, S. L. Deruiter, J. Calambokidis, A. S. Friedlaender, G. S. Schorr, D. J. Moretti, P. L. Tyack, and B. L. Southall, 2014, Using accelerometers to determine the calling behavior of tagged baleen whales.: The Journal of Experimental Biology, **217**, 2449–2455.

Gordon, J., D. Gillespie, J. Potter, A. Frantzis, M. P. Simmonds, R. Swift, and D. Thompson, 2003, A Review of the Effects of Seismic Survey on Marine Mammals: Marine Technology Society Journal, **37**, 16–34.

Groenass, H., O. P. Larsen, D. Gerez, and M. Padula, 2016, On the anatomy of the air-gun signature: Presented at the Technical Program Expanded Abstracts, Society of Exploration Geophysicists.

Hegna, S., and G. Parkes, 2011, The low frequency output of marine airgun arrays: SEG Technical Program Expanded Abstracts 2011, 77–81.

Herring, C., 1941, Theory of the pulsations of the gas bubble produced by an underwater explosion: Technical report, Office of Scientific Research and Development Report 236.

Hildebrand, J. A., 2005, Impacts of anthropogenic sound, *in* Marine mammal research: conservation beyond crisis: The John Hopkins University Press, 101–124.

Kastelein, R. A., J. Schop, R. Gransier, and L. Hoek, 2014, Frequency of greatest temporary hearing threshold shift in harbor porpoises (Phocoena phocoena) depends on the noise level: The Journal of the Acoustical Society of America, **136**, 1410–1418.

Keller, J. B., and I. I. Kolodner, 1956, Damping of underwater explosion bubble oscillations: Journal of Applied Physics, **27**, 1152–1161.

King, J. R., A. M. Ziolkowski, and M. Ruffert, 2015, Boundary conditions for simulations of oscillating bubbles using the non-linear acoustic approximation: Journal of Computational Physics, **284**, 273–290.

King, J. R. C., 2015, Air-gun bubble-ghost interactions: Geophysics, **80**, T223–T234.

Kirkwood, J. G., and H. A. Bethe, 1942, Basic propagation theory: Technical report, Office of scientific research and development.

Klüver, T., and H. Tabti, 2015, Derivation of Statistical Sea-surface Information from Dual-sensor Towed Streamer Data: 77th EAGE Conference and Exhibition 2015, 1–4.

Landrø, M., 1992, Modeling of GI gun signatures: Geophysical Prospecting, **40**, 721–747.

Landrø, M., J. Langhammer, R. Sollie, L. Amundsen, and E. Berg, 1994, Source signature determination from ministreamer data: Geophysics, **59**, 1261.

Landrø, M., and R. Sollie, 1992, Source signature determination by inversion: Geophysics, **57**, 1633–1640.

Laney, C. B., 1998, Computational gasdynamics: Cambridge University Press.

Langhammer, J., and M. Landrø, 1993, Experimental study of viscosity effects on air-gun signatures: Geophysics, **58**, 1801–1808.

———, 1996, High-speed photography of the bubble generated by an airgun: Geophysical Prospecting, 153–173.

Laws, R., M. Landrø, and L. Amundsen, 1998, An experimental comparison of three direct methods of marine source signature estimation: Geophysical Prospecting, **46**, 353–389.

Laws, R. M., L. Hatton, and M. Haartsen, 1990, Computer modelling of clustered airguns: First Break, **8**, 331–338.

Li, G., Z. Liu, J. Wang, and M. Cao, 2014, Air-gun signature modelling considering the influence of mechanical structure factors: Journal of Geophysics and Engineering, **11**.

Li, G. F., M. Q. Cao, H. L. Chen, and C. Z. Ni, 2010, Modeling air gun signatures in marine seismic exploration considering multiple physical factors: Applied Geophysics, **7**, 158–165.

Mattsson, K., 2017, Diagonal-norm upwind SBP operators: Journal of Computational Physics, **335**, 283–310.

McCauley, R. D., R. D. Day, K. M. Swadling, Q. P. Fitzgibbon, R. A. Watson, and J. M. Semmens, 2017, Widely used marine seismic survey air gun operations negatively impact zooplankton: Nature Ecology and Evolution, **1**, 1–8.

Ni, C. Z., H. L. Chen, J. Liu, Y. Q. Ye, H. X. Niu, M. Q. Cao, and Y. Liu, 2011, Parameter Optimization in Air-gun Type- dependent Signature Modeling: 73rd EAGE Conference and Exhibition, 1–4.

Nowacek, D. P., C. W. Clark, D. Mann, P. J. O. Miller, H. C. Rosenbaum, J. S. Golden, M. Jasny, J. Kraska, and B. L. Southall, 2015, Marine seismic surveys and ocean noise: time for coordinated and prudent planning: Frontiers in Ecology and the Environment, **13**, 378–386.

Orji, O. C., W. Sollner, and L. J. Gelius, 2013, Sea surface reflection coefficient estimation: SEG Technical Program Expanded Abstracts 2013, 51–55.

Pramik, B., M. L. Bell, A. Grier, and A. Lindsay, 2015, Field testing the AquaVib : an alternate marine seismic source: SEG Technical Program Expanded Abstracts 2015, 181–185.

Rayleigh, L., 1917, On the pressure developed in a liquid during the collapse of a spherical cavity: Philosophical Magazine Series 6, **34**, 94–98.

Ronen, S., and S. Chelminski, 2018, A next generation seismic source with low frequency signal and low environmental impact: 80th EAGE Conference & Exhibition, 1–5.

Southall, B. L., A. E. Bowles, W. T. Ellison, J. J. Finneran, R. L. Gentry, C. R. Greene, D. Kastak, D. R. Ketten, J. H. Miller, P. E. Nachtigall, W. J. Richardson, J. A. Thomas, and P. L. Tyack, 2008, Marine mammal noise-exposure criteria: Initial scientific recommendations: Bioacoustics, **17**, 273–275.

Stimpert, A. K., S. L. Deruiter, E. A. Falcone, J. Joseph, A. B. Douglas, D. J. Moretti, A. S. Friedlaender, J. Calambokidis, G. Gailey, P. L. Tyack, and J. A. Goldbogen, 2015, Sound production and associated behavior of tagged fin whales (Balaenoptera physalus) in the Southern California Bight: Animal Biotelemetry, **3**, 1–12.

Svärd, M., and J. Nordström, 2014, Review of summation-by-parts schemes for initial-boundary-value-problems: Journal of Computational Physics, **268**, 17–38.

Tolhoek, H. A., and S. R. de Groot, 1952, A discussion of the first law of thermodynamics for open systems: Physica, **18**, 780–790.

Vokurka, K., 1986, Comparison of Rayleigh's , Herring's , and Gilmore's Models of Gas Bubbles: Acta Acustica united with Acustica, **59**, 214–219.

Watson, L. M., E. M. Dunham, and S. Ronen, 2016, Numerical modeling of seismic airguns and low-pressure sources: SEG Technical Program Expanded Abstracts 2016, 219–224.

Watson, L. M., J. Jennings, and S. Ronen, 2017a, Source designature of ocean bottom node data using deterministic airgun modeling: SEG Technical Program Expanded Abstracts 2017, 121–126.

Watson, L. M., S. Ronen, J. A. Goldbogen, and E. M. Dunham, 2017b, Comparing whales to marine seismic sources: low frequency sound generation by fin whales: SEG Technical Program Expanded Abstracts 2017, 90–95.

Weilgart, L., 2013, A Review of the Impacts of Seismic Airgun Surveys on Marine Life: Convention on Biological Diversity Expert Workshop on Underwater Noise and its Impacts on Marine and Coastal Biodiversity, 1–10.

Williams, R., A. J. Wright, E. Ashe, L. K. Blight, R. Bruintjes, R. Canessa, C. W. Clark, S. Cullis-Suzuki, D. T. Dakin, C. Erbe, P. S. Hammond, N. D. Merchant, P. D. O'Hara, J. Purser, A. N. Radford, S. D. Simpson, L. Thomas, and M. A. Wale, 2015, Impacts of anthropogenic noise on marine life: Publication patterns, new discoveries, and future directions in research and management: Ocean and Coastal Management, **115**, 17–24.

Willis, H. F., 1941, Underwater explosions, time interval between successive explosions: Technical report.

Ziolkowski, A., 1970, A Method for Calculating the Output Pressure Waveform from an Air Gun: Geophysical Journal International, **21**, 137–161.

———, 1982, An airgun model which includes heat transfer and bubble interactions: SEG Annual Meeting, Dellas, Texas, 187–189.

Ziolkowski, A., P. Hanssen, R. Gatliff, H. Jakubowicz, A. Dobson, G. Hampson, X. Y. Li, and E. Liu, 2003, Use of low frequencies for sub-basalt imaging: Geophysical Prospecting, **51**, 169–182.

Ziolkowski, A., and G. Metselaar, 1984, The pressure wavefield of an airgun array: SEG Annual Meeting, Atlanta, Georgia, 274–276.